Interfacial coarsening dynamics in epitaxial growth with slope selection

Dorel Moldovan[1] and Leonardo Golubovic[2,*]
[1]*Materials Science Division, Argonne National Laboratory, Argonne, Illinois 60439*
[2]*Department of Physics, Harvard University, Cambridge, Massachusetts 02138*
(Received 8 November 1999)

We investigate interfacial dynamics of molecular-beam epitaxy (MBE) growth in the presence of instabilities inducing formation of pyramids. We introduce a kinetic scaling theory which provides an analytic understanding of the coarsening dynamics laws observed in numerous experiments and simulations of the MBE. We address MBE growth on crystalline surfaces with different symmetries in order to explain experimentally observed differences between the growth on (111) and (001) surfaces and understand the coarsening exponents measured on these surfaces. We supplement our kinetic scaling theory by numerical simulations which document that the edges of the pyramids, forming a network across the growing interface, are essential for qualitative understanding of the coarsening dynamics of molecular-beam epitaxy.

PACS number(s): 05.70.Ln, 68.55.−a, 05.40.−a

I. INTRODUCTION

There has been a significant research interest in the dynamics of the molecular-beam epitaxy (MBE) growth lately. The MBE technique is among the most refined methods for the growth of thin solid films and it is of great importance for applied studies [1]. By using the MBE it is possible to grow high-quality crystalline materials, and form structures with very high precision in the vertical direction, such as monolayer-thin interfaces or atomically flat surfaces.

The evolution of the surface morphology during epitaxial growth results from a delicate relation between the molecular flux and the relaxation of the surface profile through surface diffusion of adatoms. A significant factor for the adatom migration on the surface is their interaction with steps on the surface, in particular the existence of energy barriers near step edges, that inhibit the movement of atoms between layers of the growing interface. These step edge barriers, that were discovered by Ehrlich and Hudda [2] and studied by Schwoebel [3], [Ehrlich-Schwoebel energy barriers] give rise to instabilities in the evolution of the surface morphology and lead to a surface current of adatoms towards the upper step edge [4]. This instability ultimately leads to the formation of mounds and pyramids across the growing interface [5,6]. Ehrlich-Schwoebel instability is a nonequilibrium effect that is present only if the adatom density on a terrace is higher than in equilibrium. The deposition process indeed raises the adatom density far above its equilibrium value and surface currents that depend on local slope of the growing film are generated. By studying the diffusive motion of adatoms on vicinal surfaces with step-edge barriers one finds [4] that the surface nonequilibrium current $J_{\rm NE}$ has the same direction as the slope and consequently tends to increase the local slope. This is the origin of the instability. However, for sufficiently large slopes there are other processes that counterbalance the destabilizing effect, so that the net current in the *nonequilibrium* situation vanishes for certain slopes (slope selection). Transient mobility effects, such as funneling and knockout processes [7,8] can lead to zeros of $J_{\rm NE}(M)$ even for small values of the interface slope M [9,10].

As a consequence of the existence of the slope selection, the surface breaks up into pyramidlike mounds, Fig. 1(a). Pyramid facets' slopes correspond to stable zeros of the nonequilibrium surface current. Over the last few years it has become clear that the surface evolution of films grown by MBE is indeed often characterized by the formation of pyramids or pyramidlike structures, even in the case of homoepitaxial growth. These pyramidlike structures have been reported in many experiments, e.g., for homoepitaxy of GaAs [6,11], Cu [5], Ge [12], and Fe [13,14], all grown on singular (001) substrates, as well as for homoepitaxy on the Rh(111) surface [15]. What has been found in many experiments is that the lateral size λ and the height w of these pyramids grow in time as power laws with the same exponent. Thus, the ratio w/λ, corresponding to the pyramid slope, approaches a constant value at long times. Therefore, there is a slope selection in a typical MBE growth. The corresponding coarsening exponents were found from experiments to depend on the symmetry of the surface. For example, for the growth on (001) surfaces the experimental value of the coarsening exponent is close to 1/4 (in agreement with the simulations [16,17]), whereas for the growth on (111) surfaces the exponent reported was 1/3 [15].

At present, there is no real qualitative understanding of the origin of these values, or even if they are exactly 1/4 and 1/3 as they were reported from the experiments and some simulations. Our goal here is to provide *analytic explanations* of these exponents. The observation that the evolving surface morphology coarsens as more and more material is deposited is poorly understood. Here we introduce a kinetic scaling theory which provides an analytic understanding of the coarsening laws observed in experiments and simulations of the MBE growth. Our analytic theory is inspired in part by recent theories of phase-ordering processes such as the growth of domains in magnetic systems [18]. MBE growth however has a number of specific features, such that no standard phase-ordering theory could be applied to it. The

*On leave from the Physics Department, West Virginia University, Morgantown, WV 26506.

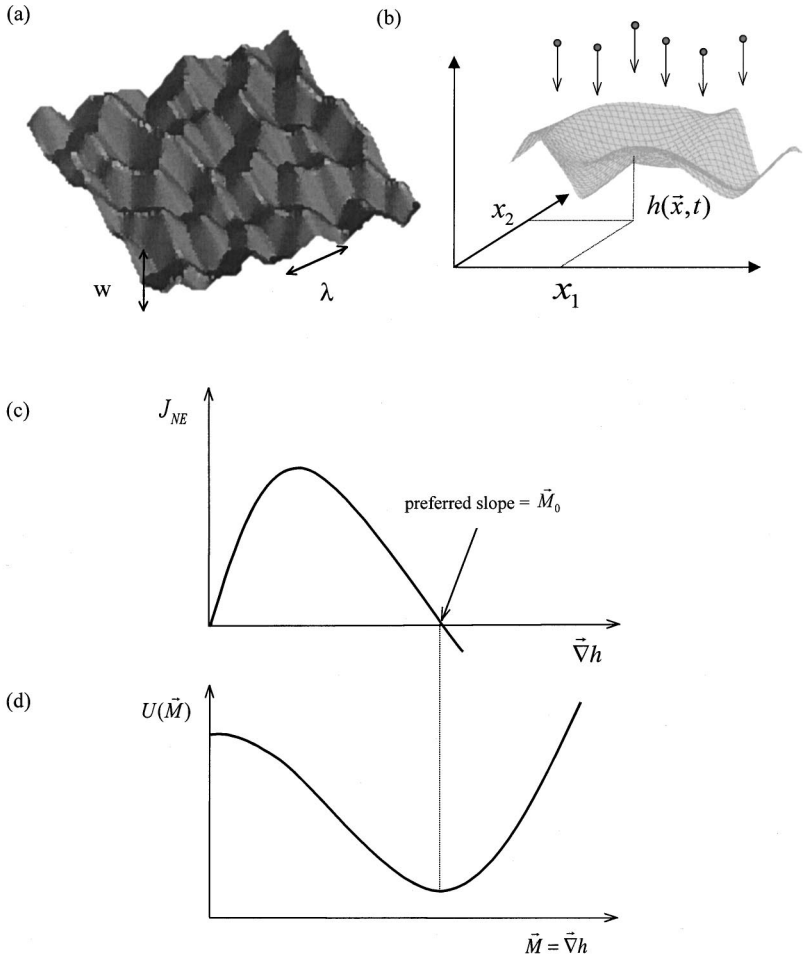

FIG. 1. (a) A snapshot of the surface from our simulations of a continuum model for the MBE growth. The two features that characterize the pyramids, the height w, and the width λ are also shown. (b) A schematic representation of the surface growth process. (c) A schematic representation of the nonequilibrium current $\mathbf{J}_{\mathrm{NE}}$ as function of the local slope $\mathbf{M}=\boldsymbol{\nabla} h$. The current makes the flat interfaces unstable to small fluctuations around the $\mathbf{M}=0$ configuration and, also, it leads to slope selection. (d) The local potential $U(\mathbf{M})$ as a function of the local slope (schematic). The value of the slope for which the local potential has the minimum corresponds to the preferred slope.

growth of mounds and pyramids arises through a subtle cooperation of surface diffusion relaxation [19] with the aforementioned effects destabilizing interfaces and selecting a preferred slope. Our analytic theory employs the fact that the interfacial dynamics is governed by an effective free energy [20,21], see Secs. II and III. In the present study we focus on the MBE growth with slope selection. Analytic theory of the MBE growth in the absence of slope selection has been developed before, in Ref. [21].

We investigate here continuum models for various types of the surface symmetry. Thus, the growth on the *isotropic* and *hexagonal* (111) symmetry surfaces was shown to exhibit a scaling behavior characterized by the presence of a single characteristic length scale $\lambda(t)=$pyramid size that grows in time as a power law, $\lambda(t)\sim t^{n_c}$. Our numerical simulations suggest that the growth of $\lambda(t)$ is governed by a coarsening exponent which assumes the *same* value for isotropic and hexagonal (111) symmetry surfaces. The coarsening exponent obtained for both cases is $n_c\cong 0.33$, see Secs. IV and V. We develop here a kinetic scaling theory that explains this scaling behavior, see Sec. VI.

Next, we elucidate the growth on the *square* symmetry (001) surfaces, see Secs. VII and VIII, and Appendix C. Because of the experimental interest, this growth has been subject of intensive numerical studies, such as the recent work of Siegert [22]. For the growth on (001) surfaces, the pyramids arrange into nearly perfectly ordered square lattices. This is best documented by looking at networks of pyramids' *edges* (lines along which pyramid facets meet) which form here a nearly perfect square lattice, see Sec. VII and Figs. 15–19 in Appendix C. Perfect periodic order of the edge lattice is disrupted by occasional presence of defects that we characterize here as *dislocations* of the edge network. These dislocations represent topological defects of (otherwise) an almost perfect square lattice of edges. The most important finding is that the interface coarsening proceeds by the *motion* of the dislocations we characterize here as the *dislocation climb* (see Secs. VII and VIII). The dislocations of edge lattices are thus crucial for the interfacial coarsening of the square symmetry (001) surfaces. The presence of dislocations causes a multiscaling behavior of the interfacial coarsening, i.e., the existence of several long length scales that grow in time with different exponents. One of them is the lateral pyramid size $\lambda(t)$ that grows as $\lambda(t)\sim t^{n_c}$, with $n_c\cong 0.25$. Other length scales are related to the presence of dislocations. They grow much faster than $\lambda(t)$. Thus, the distance between dislocations in the same row of the edge lattice $\xi(t)$ grows a $\xi(t)\sim t^{n_\xi}$. From our simulations we find $n_\xi\cong 0.5$. In this work, we develop a kinetic scaling theory that explains the coarsening exponents for the MBE growth on the square symmetry (001) surfaces, see Sec. VIII.

The layout of this paper is as follows: In Secs. II and III we discuss continuum models for the MBE growth. In Sec. IV we investigate the growth on isotropic surfaces. The growth on hexagonal symmetry (111) surfaces is studied in Sec. V. Kinetic scaling theory of the MBE growth on isotropic and hexagonal surfaces is developed in Sec. VI. The growth on square symmetry (001) surfaces is studied in Sec.

VII. Kinetic scaling theory of the MBE growth on (001) surfaces is developed in Sec. VIII. Section IX discusses various aspects of pyramid facets and edges. We summarize our findings in Sec. X. Our numerical modeling scheme is detailed in the Appendix A. Appendix B deals with the calculation of edge line tensions and edge currents. Finally, in the Appendix C we give a longer time sequence of snapshots of the edge network for the growth on square symmetry surfaces.

II. CONTINUUM MODELS FOR THE MBE GROWTH

Under conditions typical for MBE growth, the heights $h(\mathbf{x},t)$ that describe the position of the interface measured over a base plane, obey a conservation law [$\mathbf{x}=(x_1,x_2)$ is a two-dimensional base plane vector, Fig. 1(b)]. In the absence of desorbtion, vacancies or overhangs, all relaxation processes on the surface conserve the deposited volume of the growing film. Thus, in the frame comoving with the interface, the height evolution equation is of the form:

$$\frac{\partial h(\mathbf{x},t)}{\partial t}=-\boldsymbol{\nabla}\cdot\mathbf{J}+\eta(\mathbf{x},t)=-\frac{\partial J_1}{\partial x_1}-\frac{\partial J_2}{\partial x_2}+\eta(\mathbf{x},t), \quad (1)$$

where $\mathbf{J}$ is the surface current and $\eta(\mathbf{x},t)$ is the white noise describing the fluctuations of the deposition flux. The average deposition flux has been eliminated from Eq. (1) by the use of the comoving frame of reference. Noise is irrelevant in related coarsening processes such as spinodal decomposition or Ostwald ripening [18]. In the same spirit the focus of this work is on dynamics described by the Eq. (1) with $\eta(\mathbf{x},t)=0$.

The surface current $\mathbf{J}$ entering Eq. (1) can be written as a sum of two terms:

$$\mathbf{J}=\mathbf{J}_{\mathrm{SD}}+\mathbf{J}_{\mathrm{NE}}(\boldsymbol{\nabla}h). \quad (2)$$

The first term in Eq. (2) is the surface diffusion current and is present also in an equilibrium situation where it describes surface diffusion driven by surface tension [19]. The surface diffusion current has the well-known form,

$$\mathbf{J}_{\mathrm{SD}}=\kappa\boldsymbol{\nabla}(\nabla^2 h), \quad (3)$$

where κ is the surface diffusion constant [19]. The second term in Eq. (2) is the nonequilibrium diffusion current (Schwoebel term) that depends on the local slope ∇h. The form of the nonequilibrium current $\mathbf{J}_{\mathrm{NE}}(\nabla h)$ must incorporate the above-mentioned Schwoebel instability. Also, it must lead to the slope selection. For small slopes, this current is positive [4], making the initially flat interfaces unstable. However, the current may vanish and change sign at some value of the slope, see Fig. 1(c). That value will be the preferred slope.

III. FREE ENERGY FORMULATION OF THE MBE GROWTH MODEL

The continuum model of the MBE growth described in the previous section, can be put in an equivalent form which is essentially that of a type-*A* dynamics for a suitable defined effective free energy [20,21],

$$\frac{\partial h}{\partial t}=-\boldsymbol{\nabla}\cdot\mathbf{J}\Leftrightarrow\frac{\partial h(\mathbf{x},t)}{\partial t}=-\frac{\delta F_{\mathrm{eff}}}{\delta h(\mathbf{x},t)}. \quad (4)$$

Here the effective free energy F_{eff} depends on the interfacial height function $h(x_1,x_2)$ and contains two parts:

$$F_{\mathrm{eff}}=F_{\mathrm{SD}}+F_{\mathrm{NE}}. \quad (5)$$

The first term in Eq. (5) is the surface diffusion term, and it is similar to the bending energy of flexible membranes:

$$F_{\mathrm{SD}}=\frac{\kappa}{2}\int d^2x(\nabla^2 h)^2. \quad (6)$$

After taking the functional derivative of F_{SD} one recovers, in Eq. (4), the Mullins term: $\mathbf{J}_{\mathrm{SD}}=\kappa\boldsymbol{\nabla}(\nabla^2 h)$ that we have in Eq. (3). The second term in Eq. (5) contains a local potential $U(\mathbf{M})$ that depends on the slope vector $\mathbf{M}=\nabla h$ of the interface [see Fig. 1(d)], and for the continuum model has the form

$$F_{\mathrm{NE}}=\int d^2x U(\boldsymbol{\nabla}h)=\int d^2x U(\mathbf{M}). \quad (7)$$

Equations (7), (6), and (4) reduce to Eqs. (1) and (2), where the nonequilibrium current is the gradient of the potential $U(\mathbf{M})$,

$$\mathbf{J}_{\mathrm{NE}}=-\frac{\partial U(\mathbf{M})}{\partial\mathbf{M}}. \quad (7')$$

$\mathbf{J}_{\mathrm{NE}}$ vanishes at the minima of $U(\mathbf{M})$. The preferred value of the slope thus corresponds to the minimum of this local potential [see Fig. 1(d)]. Therefore, the slope vector $\mathbf{M}=\nabla h$ is an order parameter of the effective free energy F_{eff} which favors the development of growing facets with the preferred slope. Within the effective free-energy approach, Eq. (4), the development of growing pyramids, whose facet have the preferred slope, can be thus viewed as a phase-ordering process similar to those in magnetic systems. The pyramid facet size is like a magnetic domain size that grows as a power of time. If the local potential U depends just on the magnitude of the slope $|\mathbf{M}|$, that is $U(\mathbf{M})=U(|\mathbf{M}|)$, by symmetry the current will vanish on a circle in the order-parameter space (M_1,M_2), see Fig. 2(a). Such an isotropic model is not realistic for the growth on real, crystalline surfaces. For realistic surfaces with hexagonal or square symmetry, the local potential will depend both on the magnitude $|\mathbf{M}|$ and the polar angle θ of $\mathbf{M}$. Thus, $U(\mathbf{M})$ may have only a *discrete* set of minima.

For example, for the hexagonal symmetry, the local potential has the symmetry property

$$U(\mathbf{M})=U(|\mathbf{M}|,\theta)=U\left(|\mathbf{M}|,\theta+\frac{2\pi}{6}\right), \quad (8)$$

and can be thus Fourier expanded as

$$U(\mathbf{M})=U_0(|\mathbf{M}|)+U_1(|\mathbf{M}|)\cos(6\theta)+U_2(|\mathbf{M}|)\cos(12\theta)+\cdots. \quad (9)$$

By Eq. (8), $U(\mathbf{M})$ must have (at least) six minima that correspond to six preferred orientations of the facets that may appear in the growth process [see Fig. 2(b)].

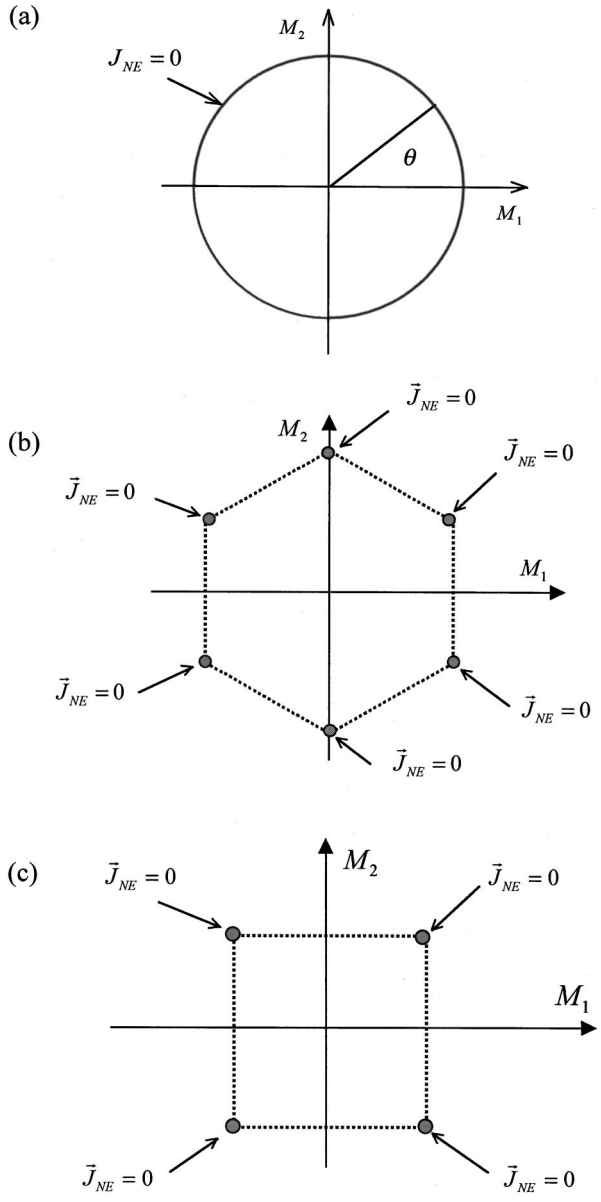

FIG. 2. (a) If the local potential $U(\mathbf{M})$ depends only on the magnitude of the local slope vector $\mathbf{M}$, the minimal value of $U(\mathbf{M})$ occurs on a circle in the order-parameter space (M_1,M_2). (b) Six minima of the local potential $U(\mathbf{M})$ for the hexagonal symmetry surfaces occur at the vertices of a hexagon in the order-parameter space (M_1,M_2). $U(\mathbf{M})$ depends both on the magnitude and the polar angle of the local slope vector $\mathbf{M}, U(\mathbf{M})=U(|\mathbf{M}|,\theta)$. The nonequilibrium current $\mathbf{J}_{\mathrm{NE}}$ vanishes at six preferred (selected) values of the slope vector with $\theta=\pi/6+(n-1)2\pi/6\,(n=1,2,...,6)$, as well at six (unstable) maxima of $U(\mathbf{M})$ (not indicated in figure) that are at $\theta=(n-1)2\pi/6\,(n=1,2,...,6)$. (c) Four minima of the local potential $U(\mathbf{M})$ for the square symmetry surfaces occur at the vertices of a square in the order-parameter space (M_1,M_2). $U(\mathbf{M})$ depends both on the magnitude and the polar angle of the local slope vector $\mathbf{M}, U(\mathbf{M})=U(|\mathbf{M}|,\theta)$. The nonequilibrium current $\mathbf{J}_{\mathrm{NE}}$ vanishes at four indicated preferred (selected) values of the slope vector, with

$$\theta=\frac{\pi}{4}+(n-1)\frac{2\pi}{4}$$

$(n=1,2,3,4)$, as well as at four (unstable) maxima of $U(\mathbf{M})$ (not indicated in the figure) that are at $\theta=(n-1)2\pi/4\,(n=1,2,3,4)$.

Likewise, for the surfaces that have square symmetry, the local potential has the symmetry property

$$U(\mathbf{M})=U(|\mathbf{M}|,\theta)=U\left(|\mathbf{M}|,\theta+\frac{2\pi}{4}\right), \tag{10}$$

and can be thus Fourier expanded as

$$U(\mathbf{M})=U_0(|\mathbf{M}|)+U_1(|\mathbf{M}|)\cos(4\theta)+U_2(|\mathbf{M}|)\cos(8\theta)+\cdots. \tag{11}$$

By Eq. (10), $U(\mathbf{M})$ must have (at least) four minima that correspond to four preferred orientations of the facets that may appear in the growth process on this type of surface [see Fig. 2(c)].

A more detailed discussion of various aspects of local potentials is given in Sec. IX.

IV. SIMULATIONS OF THE GROWTH ON THE ISOTROPIC SURFACES

Here, we present the results obtained by solving the partial differential equation that describes the growth process [see Eq. (1)] for the case of isotropic surfaces (as described in Secs. II and III). For them, the local potential $U(\mathbf{M})$ depends only on the magnitude of the slope vector $\mathbf{M}$. Thus, the set of preferred slopes is a circle in the order parameter space, see Fig. 2(a). The equation of motion is solved on a discrete grid with about 1 000 000 mesh points. The modeling scheme is detailed in Appendix A (see, also Sec. IX).

What we see from our simulation results in Fig. 3 is that the morphology of the growing interface is characterized by the development of pyramidlike structures. These are induced by the presence of the slope selection in the model. The pyramidal structures are made of nearly flat *facets* that meet at sharp *edges* (see Fig. 3). The edges carry most of the *effective free energy* F_{eff}, Eq. (5). Edges are best visualized by plotting the density of the effective free energy over the surface, as in Fig. 3(b). There, white areas correspond to the facets, and carry little effective free energy whereas dark areas are edges and carry most of the effective free energy. We can see that the edges form in fact a random mesh (network) over the surface. The characteristic size of mesh cells (pyramid facets) grows in time via a coarsening process, as it is evident from Fig. 3(b). Facets slope vectors as well as edges are *randomly* oriented. This is consistent with the isotropic nature of the model that we are simulating here. Indeed here the effective free energy is minimized by facets whose slope has a fixed magnitude, $|\nabla h|=M_0$, whereas the orientation of the facet slope vector $\mathbf{M}=\boldsymbol{\nabla} h$, can be arbitrary [energy minimum set is a circle in the order parameter space, see Fig. 2(a)]. Thus, the facets that form the pyramidlike mounds have no preferred orientation.

From Fig. 3, it is obvious that the size of the unit cell of the edge mesh $\lambda(t)$ grows with time. $\lambda(t)$ is comparable to the pyramid lateral size. Another quantity that grows with time is the width $w(t)$ of the growing interface. $w(t)$ measures the typical pyramid height. We quantify $w(t)$ as the average $[w(t)]^2=\langle[h(x,t)]^2\rangle$. Here and in the following $\langle ...\rangle$ stands for the spatial average over the base plane. In order to quantitatively characterize the surface morphology,

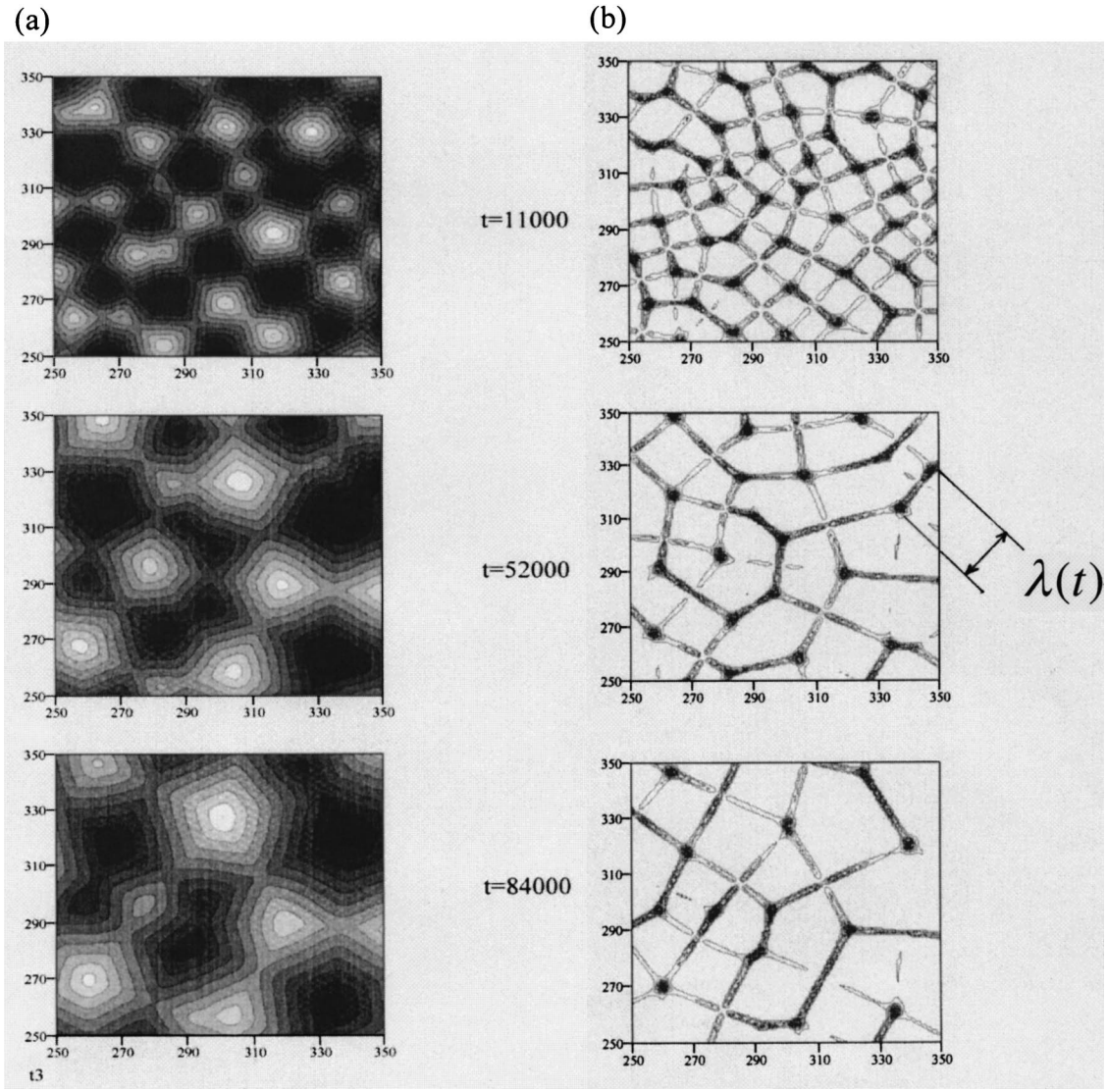

FIG. 3. (a) The contour plots that depict the time evolution of the isotropic surface. The existence of nearly flat facets bounded by edges is evident. (b) Snapshots of the edge network on a small portion (100×100) of the growing surface for the isotropic case. We can see that there is no preferred direction for the orientation of the edges. The structural length scale of the edge network $\lambda(t)$, comparable to the facet size or lateral pyramid size, grows in time.

we calculated, apart from the width $w(t)$, the height-height correlation function

$$K_{\mathrm{hh}}(r,t)=\langle h(x+r,t)h(x,t)\rangle. \tag{12}$$

$K_{\mathrm{hh}}(r,t)$ versus r has an oscillatory character reflecting the presence of mounds. We used $K_{\mathrm{hh}}(r,t)$ to find the characteristic lateral length, $\lambda(t)$ of the structure (pyramids lateral size), as the first zero crossing of the correlation function, $K_{\mathrm{hh}}(\lambda(t),t)=0$. The interface width and the lateral size of the pyramids from our simulations grow in time as power laws

$$w(t)\sim t^{\beta}, \tag{13}$$

$$\lambda(t)\sim t^{n_c}, \tag{14}$$

with the coarsening exponents

$$\beta\approx n_c=0.33\pm0.01, \tag{15}$$

as documented in Fig. 4. The fact that the coarsening exponents came out to be equal, is simply consequence of the slope selection in the model that we simulate here (the ratio w/λ represents the average slope of the facets that approaches the preferred value at long times). In Sec. VI we will give a kinetic scaling theory that explains the coarsening exponents obtained from the above simulations of the growth on the isotropic surfaces.

V. SIMULATION OF THE MBE GROWTH ON HEXAGONAL SYMMETRY (111) SURFACES

Here, we present the results obtained by solving the partial differential equation that characterizes the MBE growth process [see Eq. (1)] for the case of the growth on surfaces with hexagonal symmetry (as described in Secs. II and III). The local potential $U(\mathbf{M})$ was chosen such that it has six minima corresponding to six preferred facet orientations for this type of surfaces [see Fig. 2(b)]. The equation is solved

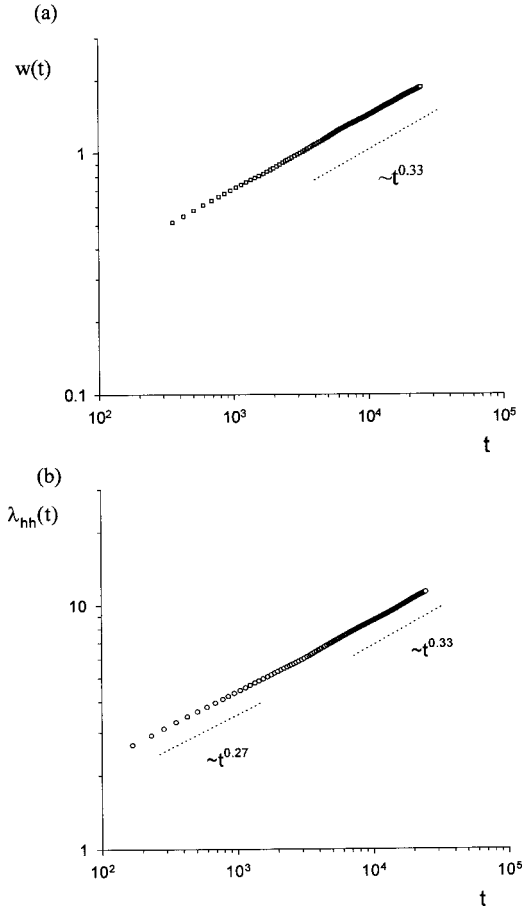

FIG. 4. (a) The width of the interface $w(t)$ versus time for the growth on the isotropic surfaces. $w(t)$ measures the typical pyramid height. The log-log plot gives the scaling $w(t)\sim t^{1/3}$ at long times. (b) Time evolution of the first zero of the height-height correlation function $K_{\rm hh}(r,t)$ called $\lambda(t)$, for the growth on the isotropic surface. $\lambda(t)$ represents the characteristic lateral size of the pyramids. The log-log plot gives the scaling $\lambda(t)\sim t^{1/3}$ at long times. $\lambda(t)$, extracted from the first zero crossing of the height-height correlation function, is just a measure of the pyramid base size. We note that such a popular qualitative measure of the pyramid size may break down under some circumstances (see, e.g., Fig. 10 below).

on a discrete grid with about 1 000 000 mesh points (see Appendix A for details of the modeling scheme).

Again, the morphology of the growing interfaces is characterized by the development of pyramidlike structures made of nearly flat facets that meet at sharp edges (see Fig. 5). The size of pyramids grows as power law of time by a coarsening process.

In contrast to the isotropic case studied in the previous section, here the edges must form a network reflecting the presence of the six preferred orientations of pyramid facets discussed in Sec. III [see Fig. 2(b)]. With the six preferred orientations for the facets in Fig. 2(b), there are $\binom{2}{6}=15$ pairs of facets. For each pair of facets, there is a distinct edge type [see Sec. IX and Appendix B]. Thus, here there are 15 types of edges selected by the anisotropy. A careful look at the edge pattern in Fig. 5(b) shows that the edges indeed point along the selected directions.

Let us look at the behavior of the interface associated with the coarsening of network of edges. We have calculated various correlation functions in order to characterize the surface morphology that we obtain from numerical simulations (see Fig. 6). One is the slope-slope correlation function $K_{MM}(r,t)$, defined as

$$K_{MM}(\mathbf{r},t)=\langle \mathbf{n}_{xy}(\mathbf{r}+\mathbf{x},t)\cdot\mathbf{n}_{xy}(\mathbf{x},t)\rangle, \tag{16}$$

where $\mathbf{n}_{xy}(\mathbf{x},t)$ are the xy (in-plane) components of the unit normal vectors $\mathbf{n}(\mathbf{x},t)$ at the point $\mathbf{x}$ on the growing surface. The other one is the height-height correlation function defined in the Eq. (12). Both $K_{\rm hh}(r,t)$ and $K_{MM}(r,t)$ versus $\mathbf{r}$ have an oscillatory character [see Figs. 6(a) and 6(b)] reflecting the presence of pyramidal mounds. The similarity with phase-ordering phenomena, discussed in Sec. III, with the slope $\mathbf{M}=\nabla h\sim\mathbf{n}_{xy}$ being an order parameter here, suggests that the slope-slope correlation functions should depend only on a single length scale, the size $\lambda(t)$ of the pyramids. Indeed, it appears that this is the case if we look at the collapse of $K_{MM}(r,t)$ correlation functions obtained at different times [see Fig. 6(a)]. On the other side, the data in Fig. 6(b) suggest a similar collapse for the height-height correlation functions.

From our simulations on the hexagonal symmetry surfaces, we find that the interface width $w(t)$, and pyramid size $\lambda(t)$, grow as $w(t)\sim\lambda(t)\sim t^{n_c}$ with $n_c\approx\frac{1}{3}$, see Figs. 6(c) and 6(d). This coarsening exponent is the *same* as that found before for the isotropic case in Sec. IV.

Numerical values of the coarsening exponents obtained above from our simulations on the hexagonal symmetry surfaces, $\beta\approx n_c\approx\frac{1}{3}$, agree well with the experimental results of Tsui and co-workers [15], for the growth on the Rh (111) surface which has the hexagonal anisotropy. We note that this is the first continuum model simulation in which the 1/3 power law has been obtained for the surfaces with *hexagonal* anisotropy. Siegert [22] recently obtained a similar 1/3 power law for the growth on surfaces with *triangular* anisotropy [such a model artificially breaks the inversion symmetry of the growth on (111) surfaces].

In the next section, we develop a kinetic scaling theory that explains the values of the coarsening exponents that we obtained both for isotropic and hexagonal symmetry surfaces. It is inspired by recent Bray's scaling theory of coarsening processes such as spinodal decomposition [18].

VI. SCALING THEORY OF THE MBE GROWTH ON ISOTROPIC AND HEXAGONAL SYMMETRY SURFACES

Here we provide analytic explanation of the 1/3 coarsening exponent obtained for the MBE growth on isotropic and hexagonal symmetry surfaces. For that purpose, we relate the dynamics of the coarsening process to the rate of extinction of the effective free-energy-rich regions. Here these energy-rich regions are the edges of the pyramids.

Consider the network of edges, depicted in Fig. 7 in terms of the density of the effective free energy in Eq. (5). The effective free energy that comes per unit cell of this edge network, with the cell size $\approx\lambda(t)$, is localized in the few edges that bound that cell. The effective free energy of an edge with a typical length λ, is proportional to the length of the edge

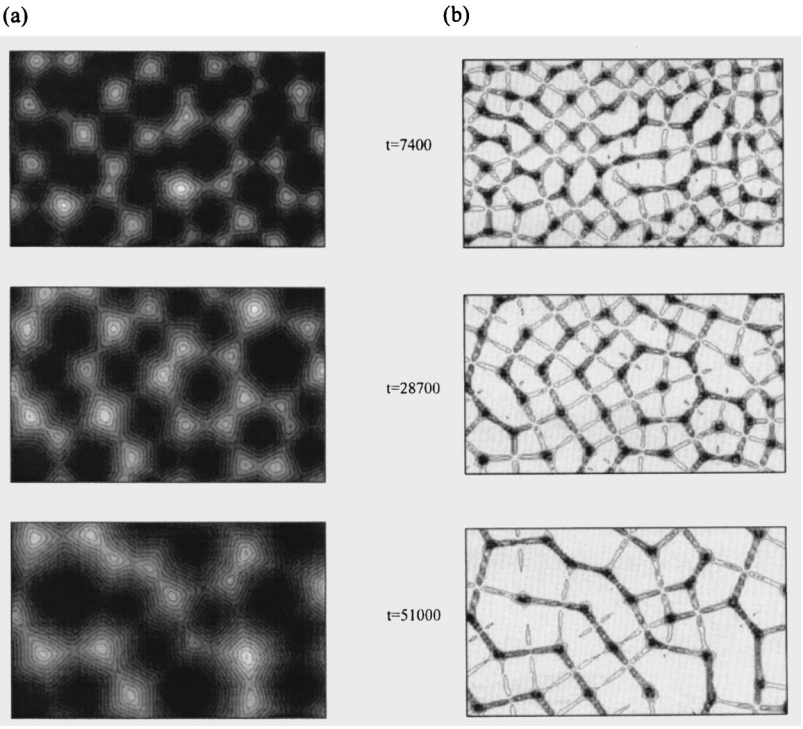

FIG. 5. (a) The contour plots that depict the time evolution of the hexagonal symmetry surfaces. Note the presence of facets bounded by edges. (b) The edge network on a small portion of the growing surface for the hexagonal symmetry surfaces. A careful look at the edges shows that their orientations are mastered by the sixfold anisotropy, as discussed in the text.

$$F_{\text{edge}}=\sigma\lambda, \tag{17}$$

where σ is the edge line tension [see Sec. IX and Appendix B]. As there is of the order of one edge per area $\sim\lambda^2$ (see Fig. 7), the effective free energy per unit area is

$$F_{\text{u.a.}}=\frac{F_{\text{eff}}}{A_B}\approx\frac{F_{\text{edge}}}{\lambda^2}=\frac{\sigma}{\lambda}, \tag{18}$$

where A_B denotes the base area of the film. Next, we use an energy relaxation equation stating that the decay of effective free energy per unit area is proportional to the spatial average of the squared interface velocity. Indeed, the equation of motion (4) implies that

$$\frac{dF_{\text{eff}}}{dt}=-\int_x\left(\frac{\partial h}{\partial t}\right)^2 d^2x. \tag{19}$$

Using Eq. (19) one can write

$$\frac{d}{dt}\frac{F_{\text{eff}}}{A_B}=-\frac{\int\left(\frac{\partial h}{\partial t}\right)^2 d^2x}{A_B}, \tag{20}$$

i.e.,

$$\frac{d}{dt}F_{\text{u.a.}}=-\left\langle\left(\frac{\partial h}{\partial t}\right)^2\right\rangle. \tag{21}$$

Using here Eq. (18) and estimating the typical velocity of the interface as

$$\left\langle\left(\frac{\partial h}{\partial t}\right)^2\right\rangle\approx\left(\frac{dw}{dt}\right)^2,$$

we get

$$\frac{d}{dt}\left(\frac{\sigma}{\lambda}\right)=-\left(\frac{dw}{dt}\right)^2.$$

If here we use the fact that $w/\lambda=M_0=$preferred slope, we further get

$$\frac{d}{dt}\left(\frac{\sigma M_0}{w}\right)=-\left(\frac{dw}{dt}\right)^2. \tag{22}$$

Equation (22) can be easily integrated yielding

$$w=M_0\lambda=\text{const}\times(M_0\sigma)^{1/3}t^{1/3}. \tag{23}$$

Therefore, we get the coarsening relations

$$w\sim\lambda\sim t^{1/3} \tag{24}$$

with the coarsening exponents $\beta=n_c=\frac{1}{3}$, which are consistent with our simulation results.

We proceed by stressing the analogies and differences between the MBE growth and phase-ordering processes, such as the domain growth in magnetic systems [18]. In the MBE growth with slope selection, the interface slope vector $\mathbf{M}=\nabla h$ develops a nonzero value and thus plays a role of an order parameter. Growing facets observed in the MBE growth are highly similar to growing domains in the phase-ordering process of Ising-type magnetic systems. Analog to a domain wall between two magnetic domains is the edge that occurs at the intersection of two nearly flat facets with different slope vectors, say $\mathbf{M}_1$ and $\mathbf{M}_2$. The edge appears as a straight line segment as evident in Figs. 3, 5, and 7. It is directed along the vector $\mathbf{M}_1+\mathbf{M}_2$ (see Sec. IX and Appendix B).

Our results call for a cautious comparison of the MBE growth with the phase-ordering phenomena in standard magnetic systems. For example, the scaling law in Eq. (24), with the coarsening exponent 1/3, turns out to be the same as that for the conserved (type B) Ising dynamics (well-known

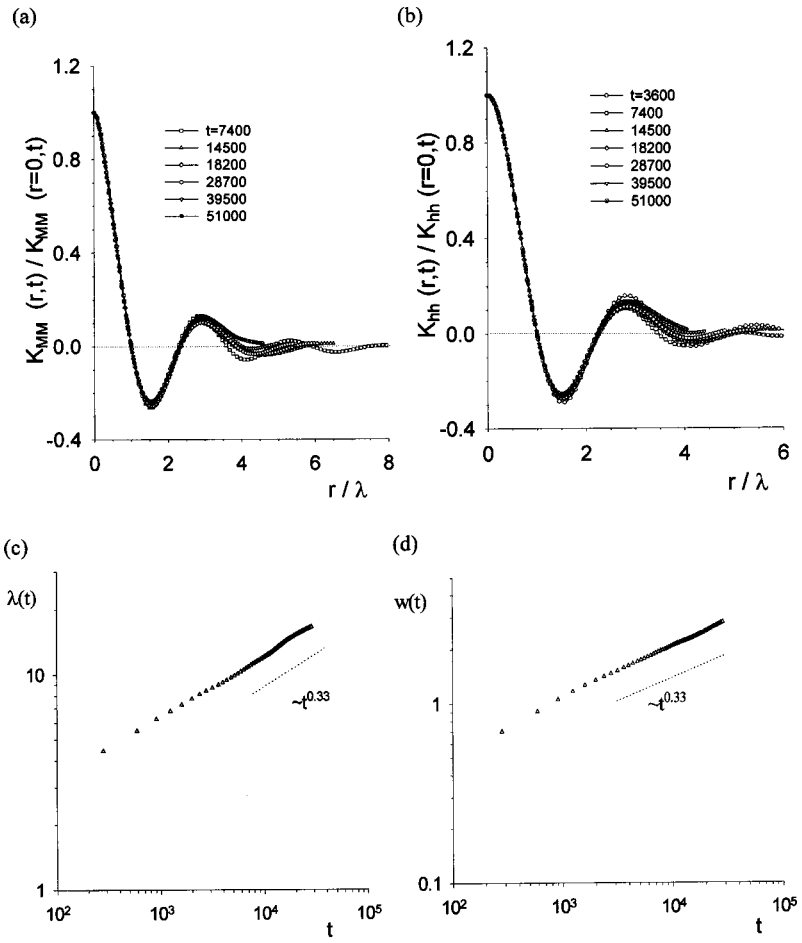

FIG. 6. (a) The collapse of the slope-slope correlation functions into a single curve $y=\psi(x)$, for hexagonal symmetry surfaces. Here $y=K_{MM}(r,t)/K_{MM}(r=0,t)$ and $x=r/\lambda_{MM}(t)$, where $\lambda_{MM}(t)$ is the first zero of $K_{MM}(r,t)$. (b) The collapse of the height-height correlation functions into a single curve $y=\psi(x)$. Here $y=K_{\rm hh}(r,t)/K_{\rm hh}(r=0,t)$ and $x=r/\lambda(t)$, where $\lambda(t)$ is the first zero of $K_{\rm hh}(r,t)$. In (a) and (b), **r** points along the nearest-neighbor bond vector of the hexagonal grid used in the numerical integration (see Appendix A). (c) Time evolution of $\lambda(t)$. $\lambda(t)$ characterizes the lateral size of the pyramids. The log-log plot gives the scaling $\lambda(t)\sim t^{1/3}$ at long times. (d) The interface width $w(t)$ versus time. The log-log plot gives the scaling $w(t)\sim t^{1/3}$ at long times.

Lifshitz-Slyozov law [18]). However, this hardly may directly explain why we find the 1/3 exponent for an *isotropic* local potential $U(\mathbf{M})$ which is invariant with respect to rotations of the slope vector **M**. This isotropic MBE model is more like an *X-Y* model than an Ising model. In fact, the MBE dynamical model is, for the isotropic case, rather similar to the conserved (type B) dynamics of an *X-Y* model which, however, has a different coarsening exponent equal to 1/4 [18]. Thus, this similarity fails to provide an understanding of the 1/3 coarsening law we find for the isotropic MBE growth.

The physical origin of this difference between the isotropic MBE model and the *X-Y* model is in the fact that, for the MBE case, the vector order parameter **M** is a gradient of another field, namely the interface height $h(x)$. With the constraint $\mathbf{M}=\nabla h$, the free energy of an *X-Y* model (two-component Ginzburg-Landau model) reduces to the effective free energy in Eqs. (5)–(7) for the isotropic case. An *X-Y* model has smeared domain boundaries and delocalized boundary free energy, with the average free-energy density given by $F_{\rm u.a.}\sim 1/\lambda^2$ rather than by the law in Eq. (18). However, in the presence of the constraint $\mathbf{M}=\nabla h$, the situation substantially changes. The domain boundaries then form as thin domain walls, edges that carry essentially all the effective free energy of the system. This *energy localization*, similar to that in Ising systems, eventually yields the law $F_{\rm u.a.}\sim 1/\lambda$, as in Eq. (18), which is crucial for obtaining the 1/3 coarsening law in Eq. (24).

We emphasize that this energy localization, i.e., the existence of facets bounded by edges is *by no means* conditioned by the presence of anisotropies. In fact, the edges and the associated 1/3 coarsening power law do exist even for the isotropic MBE growth, as documented by simulations in Sec. IV. A long edge is simply a stable stationary solution of evolution equation (4), for which $\delta F_{\rm eff}/\delta h=0$. This equation has edge-type solutions even for the isotropic MBE growth models, as detailed in Sec. IX and Appendix B.

This feature is in marked contrast to ordinary *X-Y* systems. There, sharp domain walls occur *only* in the presence

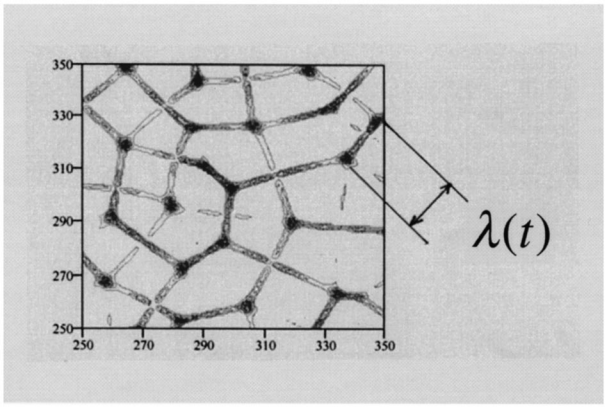

FIG. 7. The network of edges for a smaller portion (100 $\times$100) of the isotropic surface. The characteristic length of the edges $\sim\lambda(t)$, the pyramid size.

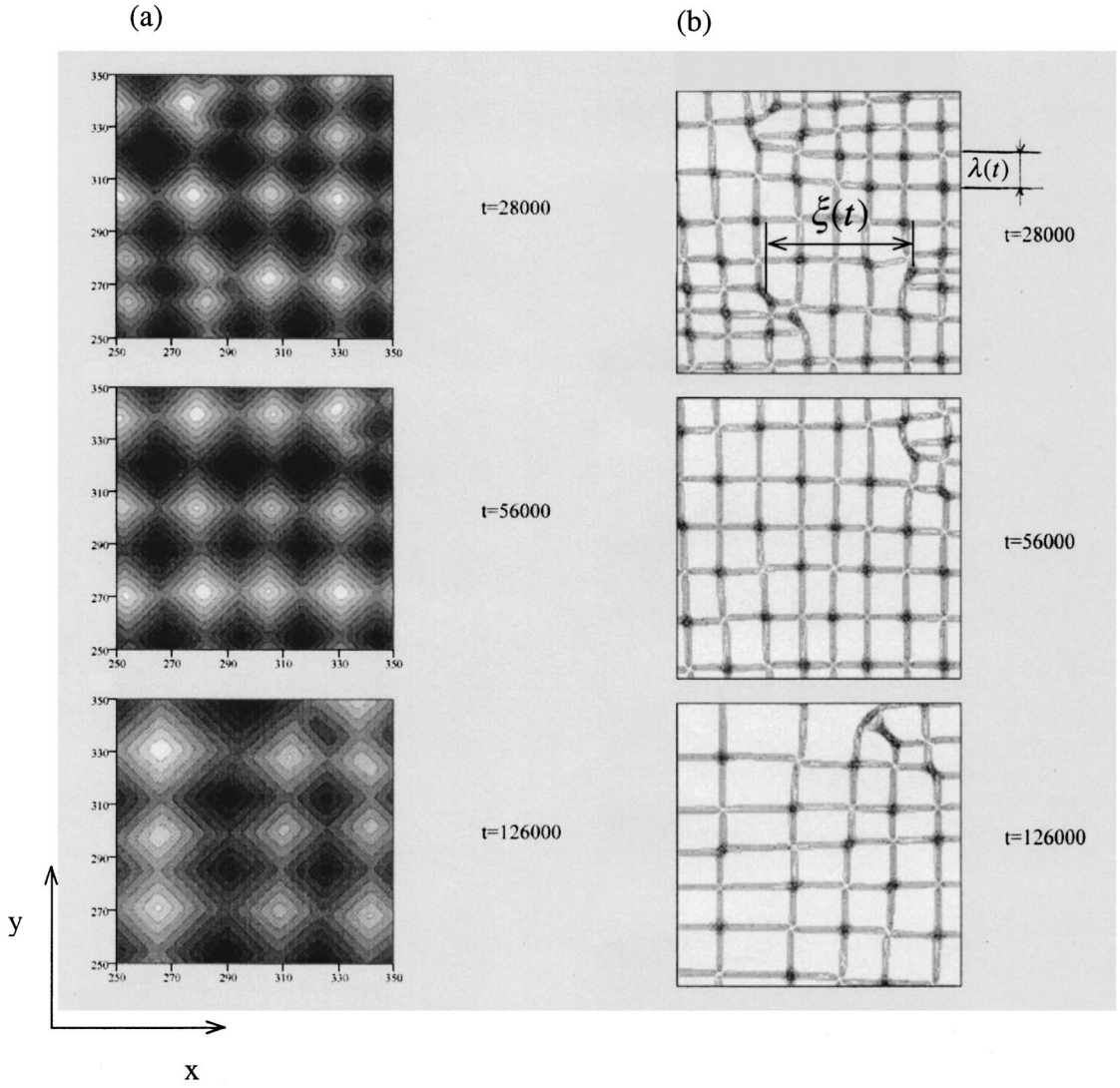

FIG. 8. (a) The contour plots that depict the time evolution of the square anisotropy surfaces, like (001). Almost regular lattice of four sided pyramids is clearly visible. (b) Three snapshots of the edge lattice of a small portion of the growing surface for the square anisotropy surfaces. We see the presence of dislocations, which are topological defects of the edge lattice. Each dislocation incorporates a rooftop edge. Dislocations move, and their motion mediates coarsening, as explained in the text.

of anisotropies. However, the isotropic MBE model has sharp domain walls (edges) and energy localization *even in the absence of spatial anisotropies* such as the hexagonal anisotropy discussed before. The observed 1/3 coarsening power law, for the isotropic MBE model, is a direct consequence of this energy localization implying the law $F_{\text{u.a.}} \sim 1/\lambda$ rather than the law $F_{\text{u.a.}} \sim 1/\lambda^2$ that applies to the isotropic *X*-*Y* model [and yields there the 1/4 corsening law for the conserved (type B) dynamics].

How does the presence of anisotropies modify this 1/3 coarsening power law? A crucial feature for this law, that $F_{\text{edge}} \sim \lambda$ and thus $F_{\text{u.a.}} \sim 1/\lambda$, will not be altered by the presence of anisotropies. Thus, one could expect that the 1/3 coarsening power law may be preserved in the presence of anisotropies. This is apparently the case for the hexagonal anisotropy studied in Sec. V. For this case, the anisotropy orients the edges. Nonetheless, the resulting edge networks are still essentially random, like those of the isotropic case, cf. Figs. 3 and 5. No strong constraints on the edge dynamics are imposed in such random networks, and the coarsening goes with the same power law as in the isotropic case. On the other side, as discussed in the next section, *square anisotropy* may induce formation of more regular edge structures, ''edge crystals,'' that impose special constraints on the edge dynamics. For such situations, the basic 1/3 coarsening power law may break down, as detailed in the following.

VII. MBE GROWTH ON SQUARE SYMMETRY (001) SURFACES

In this and the following section, we study the MBE growth on square symmetry (001) surfaces. To check for finite-size effects we simulated systems with three different sizes 500×500, 700×700 and 1000×1000 mesh points of the integration grid. The local potential $U(\mathbf{M})$ was chosen such that it has a square symmetry, with the nonequilibrium current vanishing at four minima of $U(\mathbf{M})$ as in Fig. 2(c). The modeling scheme is detailed in Appendix A (see, also Sec. IX).

Looking at the simulation results in Fig. 8 we see that the

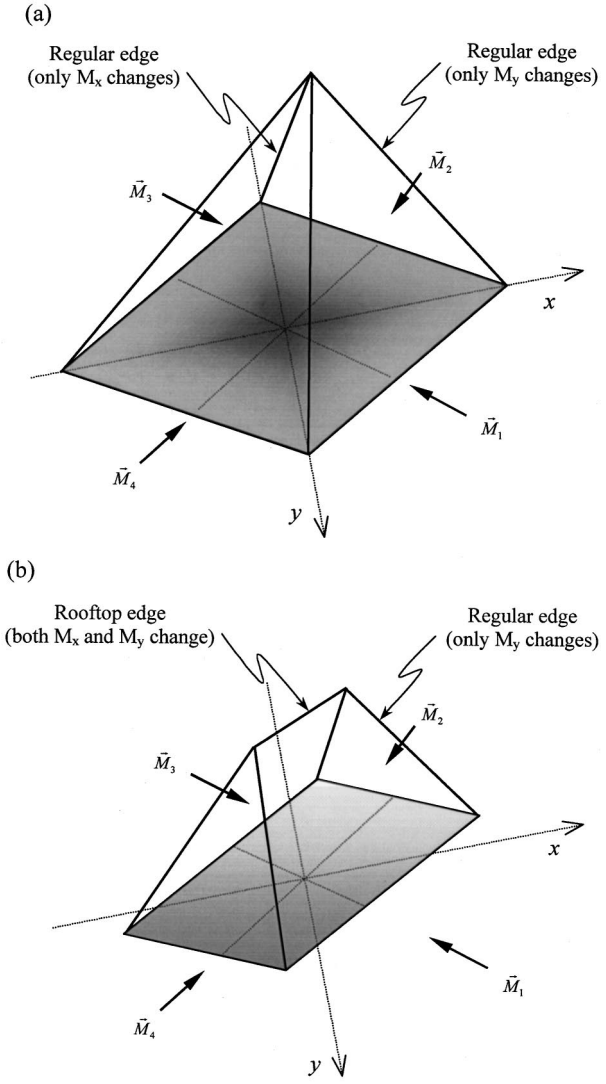

FIG. 9. (a) Regular edges. Here $\mathbf{M}_1,\mathbf{M}_2,\mathbf{M}_3,\mathbf{M}_4$ indicate the four preferred slope vectors. Note that at regular edges only one component of $\mathbf{M}$ (either x or y component) changes in sign. (b) Rooftop edge. As in (a), here $\mathbf{M}_1,\mathbf{M}_2,\mathbf{M}_3,\mathbf{M}_4$ indicate the four preferred slope vectors. Note that at rooftop edges both components of $\mathbf{M}$ are changing in sign, i.e., $\mathbf{M}\rightarrow-\mathbf{M}$.

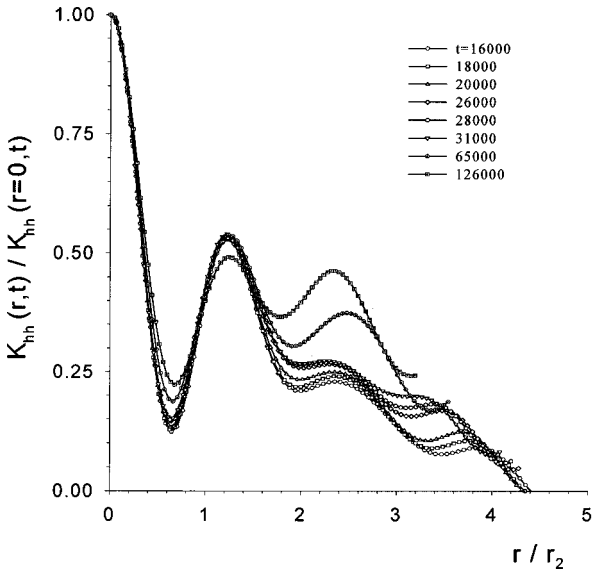

FIG. 10. The collapse trial of the height-height correlation functions into a single curve $y=\psi(x)$, for the square anisotropy (001) surfaces. Here $y=K_{\mathrm{hh}}(r,t)/K_{\mathrm{hh}}(r=0,t)$, and $x=r/r_0(t)$, where $r_0(t)$ is the position of the midpoint between the first minimum and the second maximum of the correlation function. Here, the correlations are given for the x direction, $\mathbf{r}=(x,0)$. Note that, in contrast to $r_0(t)$, the first zero crossing of this correlation function (measured along the x direction) both qualitatively and quantitatively fails to represent a measure of the actual pyramid size.

presence of square anisotropy reflects on the pyramids strongly: the pyramid facets slopes are well oriented along the four preferred directions in Fig. 2(c). Moreover, if we look across the growing interface [see Fig. 8(b) and Figs. 15–19 in Appendix C], we see the presence of a highly ordered network of edges. There are two types of edges that appear with the square anisotropy:

(a) Regular edges, oriented parallel to the x or y axis: At them, *only* one component of the facet slope vector $\mathbf{M}=\boldsymbol{\nabla}h$ changes in sign; either $(M_x,M_y)\rightarrow(-M_x,M_y)$ or $(M_x,M_y)\rightarrow(M_x,-M_y)$ see Fig. 9(a).

(b) Rooftop edges, oriented parallel to $y=\pm x$ axis: At them, both components of the facet slope vector $\mathbf{M}=\boldsymbol{\nabla}h$ change in sign; $(M_x,M_y)\rightarrow(-M_x,-M_y)$, see Fig. 9(b).

Figure 8 as well as the figures given in the Appendix C, give the details of the coarsening process for the square anisotropy surfaces. Particularly informative are the figures with edge structures [Fig. 8(b) and Figs. 15–19 in Appendix C]. From them we see that the edge network forms as a nearly regular square lattice, ''edge crystal'' with the lattice constant$=\lambda(t)$. Another feature is the marked presence of *dislocations* moving through this lattice of edges, see Fig. 8(b) and the Figs. 15–19 in Appendix C. We see that the *dislocations mediate the coarsening process*, i.e., the increase of the edge lattice constant $\lambda(t)$ in time. Indeed, by looking at the dislocation in the upper part of Fig. 8(b) we can see that this is the case. This dislocation apparently moves to the right. This motion goes on via gradual extinction (collapse) of two horizontal lines of edges terminating at the dislocation core [see Fig. 8(b), the horizontal lines terminating at the rooftop ridge in the dislocation core]. In effect, the *total* length of edges in the system decreases and pyramid facets thus grow: Note the presence of *larger* facets just to the left of the dislocation core and *smaller* facets to the right of the dislocation in the Fig. 8(b). As the two horizontal edges terminating at the dislocation core collapse, the three smaller facets transform into one larger facet, and, at the same time, the dislocation moves to the right. Thus, the coarsening process is mediated by the dislocation motion.

Another manifest feature in Fig. 8(b) and in Figs. 15–19 in Appendix C, is the presence of physical length scales *different* from $\lambda(t)$. In Fig. 8(b), we indicated another length scale, called there as $\xi(t)$, which represents the distance between two neighboring dislocations measured along the x direction. See, e.g., the two dislocations in the bottom part of Fig. 8(b) at $t=28\,000$. Subsequently, the left dislocation moves to the left whereas the right dislocation moves to the right. Thus, $\xi(t)$ increases in time.

In order to characterize the surface morphology, we calculate four types of correlation functions (see Figs. 10 and

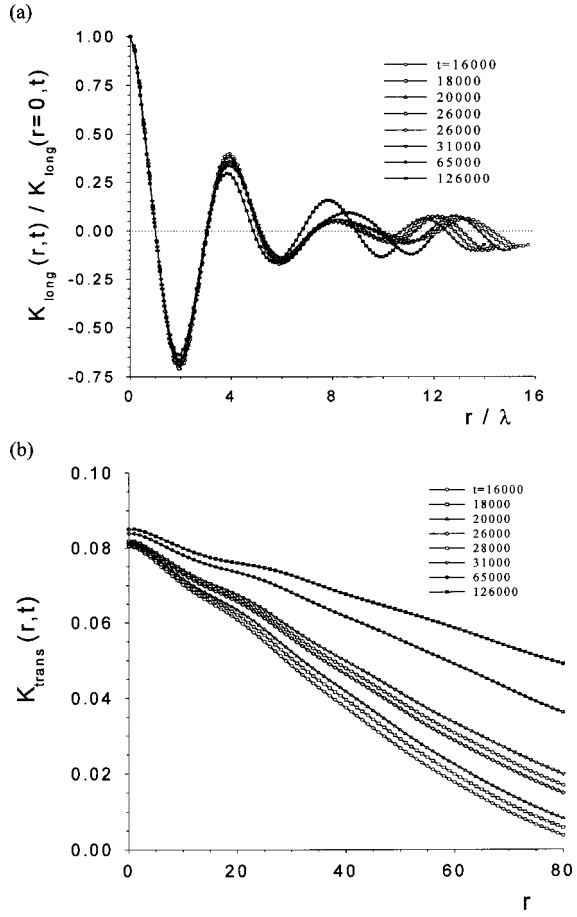

FIG. 11. (a) The trial collapse of the longitudinal slope-slope correlation functions into a single curve $y=\psi(x)$, for the square anisotropy (001) surfaces. Here $y=K_{\rm long}(r,t)/K_{\rm long}(r=0,t)$ and $x=r/\lambda(t)$, where $\lambda(t)$ is the position of the first zero crossing of the correlation function. (b) The transverse slope-slope correlation function $K_{\rm trans}(r,t)$ at various times for the growth on the square anisotropy (001) surfaces.

11). The first of them is the equal time height-height correlation function defined by

$$K_{\rm hh}(r,t)=\langle h(x+r,y,t)\cdot h(x,y,t)\rangle. \tag{25}$$

As for the growth on hexagonal surfaces, this correlation function has an oscillatory character reflecting the presence of the periodic structure of mounds, see Fig. 10. We tried to see if the height-height correlation functions, obtained at different times for the square anisotropy surfaces, collapse into a single curve, see Fig. 10. Apparently, the collapse trial fails. Closely related height-height difference correlation functions

$$K_{\rm hh\text{-}diff}(r,t)=\langle (h(x+r,y,t)-h(x,y,t))^2\rangle \tag{26}$$

would thus also fail to collapse. The reason for the failure of the collapse of these correlation functions is in the existence of several large lengthscales. Indeed, as noted above, in addition to the pyramid facet size $\lambda(t)$, we have another length scale $\xi(t)$ measuring the distance between neighboring dislocations along the x direction.

Looking at the structure of the network of edges, one can define two other correlation functions that would capture the length scales $\lambda(t)$ and $\xi(t)$:

(i) The *longitudinal* slope-slope correlation function defined as

$$K_{\rm long}(r,t)=\langle M_x(x,y,t)\cdot M_x(x+r,y,t)\rangle, \tag{27}$$

where, $M_x(x,y,t)=\partial h/\partial x=h(x+1,y,t)-h(x,y,t)$ is the x component of the local slope.

(ii) The *transverse* slope-slope correlation functions defined as

$$K_{\rm trans}(r,t)=\langle M_y(x,y,t)\cdot M_y(x+r,y,t)\rangle, \tag{28}$$

where $M_y(x,y,t)=\partial h/\partial y=h(x,y+1,t)-h(x,y,t)$ is the y component of the local slope.

To understand how the correlation functions in Eqs. (27) and (28) behave, consider variations of $M_x(x,y)$ and $M_y(x,y)$ along a horizontal line ($y=$const) in Fig. 8(b). By moving along this line one is crossing both the regular edges (where M_x changes sign and M_y remains unchanged) and the rooftop edges incorporated in the dislocation cores (where both M_x and M_y change sign). Thus, along the line $y=$const, $M_x(x,y)$ changes sign as x is increased by $\Delta x\approx\lambda=$the distance between neighboring regular edges. In effect, the correlation function of M_x in Eq. (27) is dominated by the length scale λ. On the other side, $M_y(x,y)$ changes sign only if x is increased by $\Delta x\approx\xi=$the separation between two neighboring dislocations measured the x direction. Thus, the correlation function of M_y in Eq. (28) will be mostly sensitive only to the length scale ξ being the average separation between the dislocations in the same row of the ridge lattice.

As can be seen from simulations [see Fig. 11(a)], correlation functions of M_x in Eq. (27) have an oscillatory character reflecting evenly spaced regular edges at the distance $\approx\lambda$, that can be determined from the first zero crossing of this correlation function. We used this to extract $\lambda(t)$ versus time, see Fig. 12(a). On the other side, as documented by our simulations [see Fig. 11(b)], the correlation function of M_y in Eq. (28), decays to zero at a distance $\sim\xi$. This correlation function has no oscillatory character because the dislocations are randomly placed along the x axis, with the average distance between neighboring dislocations equal to ξ. The length scale ξ can be conveniently defined as the distance at which the transverse correlation function (28) decays to one half of its value at the origin, i.e., $K_{\rm trans}[r=\xi(t),t]=\frac{1}{2}K_{\rm trans}(r=0,t)$. We used this to extract $\xi(t)$ versus time, see Fig. 12(b). Apart from $\lambda(t)$ and $\xi(t)$, we calculated also the interface width $w(t)$, see Fig. 12 (c). From data in Fig. 12, we obtain

$$w(t)\sim t^{\beta}, \tag{29}$$

$$\lambda(t)\sim t^{n_c}, \tag{30}$$

$$\xi(t)\sim t^{n_\xi}, \tag{31}$$

with the coarsening exponents

$$n_c=0.22\pm0.01\approx\beta=0.24\pm0.01, \tag{32}$$

$$n_\xi=0.50\pm0.02. \tag{33}$$

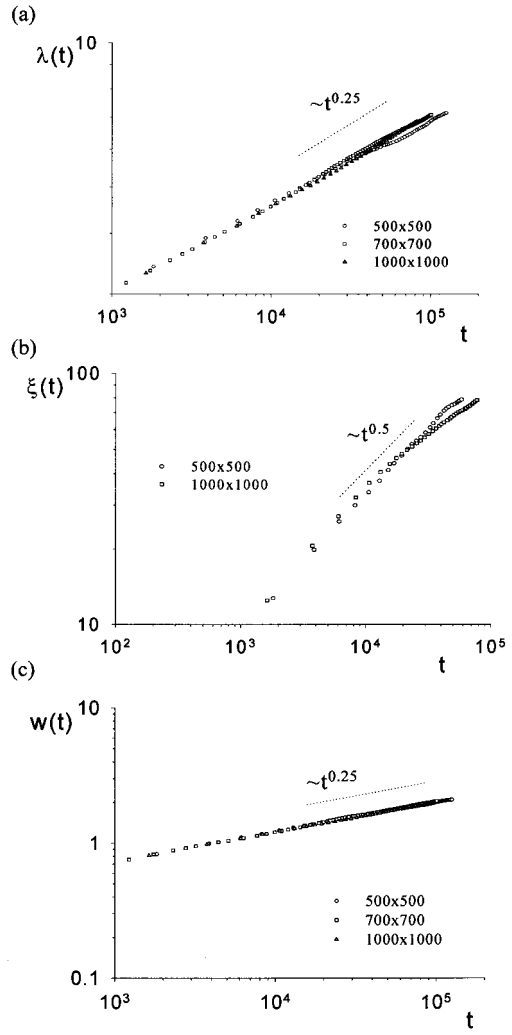

FIG. 12. (a) Time evolution of $\lambda(t)$, the first zero of the longitudinal slope-slope correlation function $K_{\text{long}}(r,t)$, for the growth on the square anisotropy (001) surfaces. $\lambda(t)$ measures the average size of the pyramids. (b) Time evolution of $\xi(t)$, the average distance between neighboring dislocations along the x direction. $\xi(t)$ is obtained from the transverse slope-slope correlation function $K_{\text{trans}}(r,t)$, as described in the text. (c) The interface width versus time for the growth on the square anisotropy (001) surfaces. The log-log plot gives the scaling $w(t) \sim t^{1/4}$ at long times. All data are given for several different system sizes (500×500, 700×700 and 1000×1000).

As n_ξ is bigger than n_c, the distance between two neighboring dislocations, along the x direction, $\xi(t)$, is much larger than the pyramid size $\lambda(t)$. By Eqs. (30) and (31), $\xi \sim \lambda^{n_\xi/n_c}$, with $n_\xi/n_c \approx 2$. Due to this, the calculation of $\xi(t)$ is more sensitive to the finite-size effects [as can be seen from Fig. 12(b)].

In the next section we propose a kinetic scaling theory for the MBE growth on the surfaces with square anisotropy. It is based on the physical picture obtained from our simulations, with two major ingredients: (i) As noted at the beginning of this section, the coarsening, i.e., increase of $\lambda(t)$ with time is mediated by dislocations of the edge lattice moving along x (or y) direction, in a fashion called as ''dislocation climb'' in the literature on dislocations in standard (atomic) lattices. (ii) Moving dislocations can meet each other and *annihilate*. This is documented in the figures of edge networks presented in the Appendix C, see Figs. 15–19.

VIII. KINETIC SCALING THEORY OF THE MBE GROWTH ON THE SQUARE ANISOTROPY (001) SURFACES

As described in the previous section and summarized in Fig. 13(a), the coarsening on the square anisotropy (001) surfaces is characterized by the presence of two characteristic length scales. One of them $\lambda(t)$ is the lattice constant of the edge lattice. $\lambda(t)$ thus measures the lateral size of the four sided pyramids. The other length scale, $\xi(t)$ is the characteristic distance between two dislocations of the edge lattice along the x direction (or y direction). These two characteristic length scales grow in time as power laws [see Eqs. (30) and (31)] with different coarsening exponents n_c and n_ξ that we obtained from our simulations. They suggest $n_c \approx \beta \approx \frac{1}{4}$, whereas $n_\xi \approx \frac{1}{2}$.

Surprisingly, the usually made assumption that there is only a single length scale and that correlation functions, therefore, follow a simple scaling law was not really questioned until recently [22]. Though values of the coarsening exponents for the pyramids size $n_c \approx \beta \approx \frac{1}{4}$ were reported in previous numerical simulations [16,17] and in the experiments on (001) surfaces, analytic theories that attempt to explain this exponent are so far not developed. In the following, we develop a kinetic theory for the coarsening process on (001) surfaces that carefully takes into account the existence of two large length scales, $\lambda(t)$ and $\xi(t)$.

As noticed in Sec. VII, the coarsening on the square symmetry surfaces is mediated by the dislocations of the edge lattice. In the previous section, we saw that the edge lattice coarsens during the motion (climb) of these dislocations along the x or y direction. Let N_{disl} denote the total number of dislocations moving along the x direction. Their density per unit area is

$$n_{\text{disl}} = \frac{N_{\text{disl}}}{A_B}, \tag{34}$$

where A_B denotes the base area of the film. The length scale ξ is the average distance between the dislocations in the *same* lattice row of the height λ, as schematized in Fig. 13(a). Thus, there is just one dislocation on a rectangle with the height $=\lambda$ and width $=\xi$ [see Fig. 13(a)]. So $n_{\text{disl}}\lambda\xi = 1$, i.e.,

$$n_{\text{disl}} = \frac{1}{\lambda\xi}. \tag{35}$$

Let L denote the *total* length of the edges which are directed along the x direction. On an L_x by L_y substrate ($A_B = L_x \cdot L_y$), one has $L = L_x \times$ *number of rows* $= L_x(L_y/\lambda)$. Thus,

$$L = \frac{A_B}{\lambda}. \tag{36}$$

During the motion of each dislocation, with velocity v_{disl}, the length L decreases during the time dt, by the amount equal to $2v_{\text{disl}}dt$. The factor of 2 here is due to having two lines of edges that are along the x direction and terminate at each

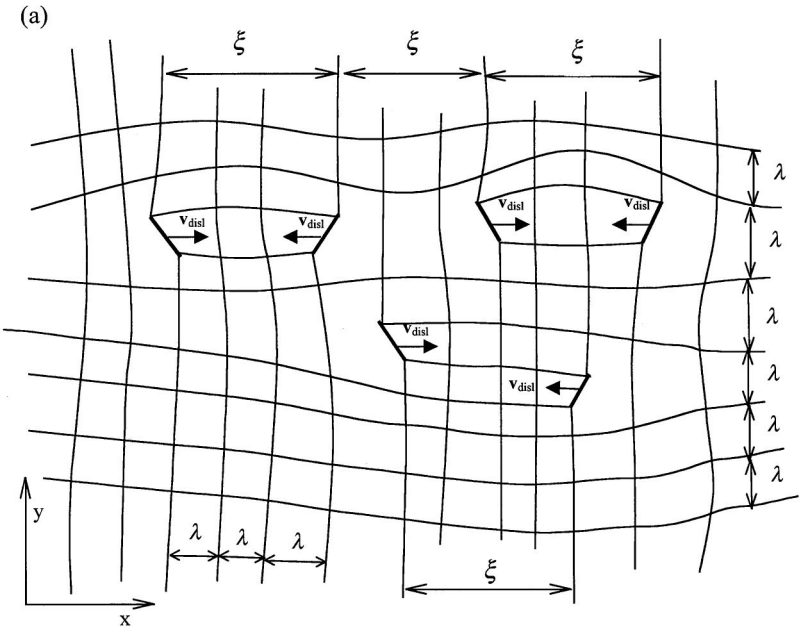

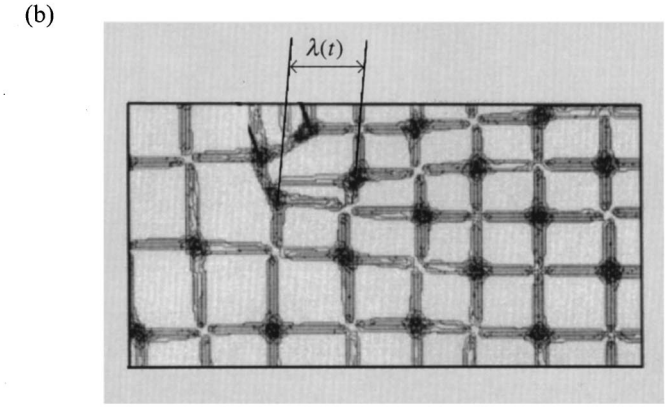

FIG. 13. (a) A schematic representation of the moving dislocations of the edge lattice and their motion. Note that dislocations may annihilate with opposite dislocations moving either in the same row or neighboring rows of the edge lattice. (b) A small portion (100×100) of the lattice of edges for the square anisotropy surfaces. The dislocation core size is $\approx\lambda$.

dislocation core [see Fig. 13(a)]. As there are $N_{\rm disl}$ moving in the x direction, the total change of L is

$$dL=-N_{\rm disl}2v_{\rm disl}dt. \tag{37}$$

Thus,

$$\frac{dL}{dt}=-N_{\rm disl}2v_{\rm disl}. \tag{38}$$

Using Eqs. (38) and (36)

$$\frac{d(A_B/\lambda)}{dt}=-N_{\rm disl}2v_{\rm disl}, \tag{39}$$

$$\frac{d(1/\lambda)}{dt}=-\frac{N_{\rm disl}}{A_B}2v_{\rm disl}. \tag{40}$$

Using here $n_{\rm disl}=N_{\rm disl}/A_B$,

$$-\frac{1}{\lambda^2}\frac{d\lambda}{dt}=-2n_{\rm disl}v_{\rm disl}. \tag{41}$$

Using here Eq. (35) for the dislocation density $n_{\rm disl}$ we have

$$\frac{1}{\lambda}\frac{d\lambda}{dt}=2\frac{v_{\rm disl}}{\xi}. \tag{42}$$

The total number of the dislocations, $N_{\rm disl}$ decreases in time due to annihilations with other dislocations [see Figs. 15–19 in Appendix C]. Thus, one can write

$$\frac{1}{N_{\rm disl}}\frac{dN_{\rm disl}}{dt}=-\frac{1}{\tau},$$

i.e.,

$$\frac{1}{n_{\rm disl}}\frac{dn_{\rm disl}}{dt}=-\frac{1}{\tau}, \tag{43}$$

where τ is the mean lifetime of a dislocation before it annihilates with another dislocation. For example, a pair of opposite dislocations moving in the same row, with relative velocity $2v_{\rm disl}$, annihilates after typical time $\tau=\xi/2v_{\rm disl}$ [see Fig. 13(a)]. By taking into account only this annihilation channel one would thus obtain

$$\frac{1}{\tau}=\frac{2v_{\rm disl}}{\xi}. \tag{44}$$

However, Eq. (44) takes into account just one possible channel of dislocation annihilations. A dislocation may annihilate also with apposite dislocations moving in the rows *above* and *below* the row in which the dislocation is moving [see Fig.

13(a)]. Thus, instead of just one, there are $q=3$ channels of dislocation annihilations. The total rate of annihilations is thus q times bigger than that in Eq. (44), i.e.,

$$\frac{1}{\tau}=q\frac{2v_{\rm disl}}{\xi}, \tag{45}$$

with $q=3$. Using (45) and (43),

$$\frac{1}{n_{\rm disl}}\frac{dn_{\rm disl}}{dt}=-q\frac{2v_{\rm disl}}{\xi}. \tag{46}$$

With Eqs. (46) and (35),

$$-\frac{1}{\xi}\frac{d\xi}{dt}-\frac{1}{\lambda}\frac{d\lambda}{dt}=-q\frac{2v_{\rm disl}}{\xi}. \tag{47}$$

Using here Eq. (42),

$$\frac{1}{\xi}\frac{d\xi}{dt}=(q-1)\frac{2v_{\rm disl}}{\xi}. \tag{48}$$

With Eqs. (48) and (42),

$$\frac{\frac{1}{\xi}\frac{d\xi}{dt}}{\frac{1}{\lambda}\frac{d\lambda}{dt}}=\frac{d(\ln\xi)}{d(\ln\lambda)}=q-1. \tag{49}$$

Integrating Eq. (49) gives

$$\xi\sim\lambda^{q-1}, \tag{50}$$

i.e., with $q=3$, $\xi\sim\lambda^2$. To proceed, we will use the relation

$$v_{\rm disl}\sim\frac{1}{\lambda^2}, \tag{51}$$

stating that the dislocation velocity is inversely proportional to the square of the lattice constant λ of the edge lattice (as discussed later on). Using Eqs. (51) and (42) we obtain

$$\frac{1}{\lambda}\frac{d\lambda}{dt}=\frac{2v_{\rm disl}}{\xi}\sim\frac{1}{\xi\lambda^2}. \tag{52}$$

By combining Eqs. (50) and (52),

$$\frac{1}{\lambda}\frac{d\lambda}{dt}\sim\frac{1}{\lambda^{q+1}}. \tag{53}$$

Integrating Eq. (53) yields

$$\lambda(t)\sim t^{1/(q+1)}. \tag{54}$$

Using Eqs. (54) and (50) we get another scaling relation

$$\xi(t)\sim t^{(q-1)/(q+1)}. \tag{55}$$

Equations (54) and (55) state that $\lambda(t)\sim t^{n_c}$ and $\xi(t)\sim t^{n_\xi}$, with

$$n_c=\frac{1}{q+1}, \tag{56}$$

$$n_\xi=\frac{q-1}{q+1}. \tag{57}$$

Recalling here that there are three channels of dislocation annihilations, $q=3$, we get the following values for the coarsening exponents:

$$n_c=\frac{1}{4}\quad\text{and}\quad n_\xi=\frac{1}{2}. \tag{58}$$

These analytically derived values of the coarsening exponents are in agreement with the results obtained from the numerical simulations of the MBE growth on square anisotropy surfaces. We note that the average distance between dislocations (in *any* direction),

$$d=\frac{1}{\sqrt{n_{\rm disl}}}, \tag{59}$$

is different from the length scale ξ, which measures the average distance between neighboring dislocations in the same row of the edge lattice [i.e., along the x axis]. Indeed, using Eqs. (59) and (35),

$$d=\sqrt{\xi\cdot\lambda}. \tag{60}$$

Thus, $d\sim t^{n_d}$, with

$$n_d=\frac{n_\xi+n_\lambda}{2}. \tag{61}$$

With Eq. (58),

$$n_d=\frac{3}{8}=0.375. \tag{62}$$

We noted before [see Eq. (51)] that the dislocation velocity $v_{\rm disl}$ is inversely proportional to the square of the lattice constant λ of the edge lattice. To see this, consider the dislocation in Fig. 13(b). One has $v_{\rm disl}=\lambda/t_1(\lambda)$, where $t_1(\lambda)$ is the time needed for a dislocation to move distance$=\lambda$. During this move, the two edges just above and below the dislocation core, merge and are extinct. After this extinction, the dislocation in Fig. 13(b) moves the distance$=\lambda$ to the right. The time $t_1(\lambda)$ it takes for this process to occur is related to λ via $\lambda\sim(t_1)^{1/3}$, as one can infer by considering this edge extinction event along the reasoning that lead us to Eq. (24). Thus $t_1\sim\lambda^3$, and $v_{\rm disl}=\lambda/t_1\sim1/\lambda^2$, as anticipated before in Eq. (51).

IX. FACETS, EDGES, EDGE TENSIONS, AND EDGE CURRENTS

Formation of nearly flat facets, bounded by straight edges, is the major feature of the epitaxial growth with slope selection. This feature is directly related to the effective free-energy approach to MBE growth [21], see Sec. III. Indeed, the interface evolution is governed by the effective free energy in Eqs. (5) to (7), that is,

$$F_{\rm eff}=\int d^2x\left[U(\boldsymbol{\nabla}h)+\frac{\kappa}{2}(\nabla^2h)^2\right], \tag{63}$$

via the type-A dynamics,

$$\frac{\partial h(\mathbf{x},t)}{\partial t}=-\frac{\delta F_{\rm eff}}{\partial h(\mathbf{x},t)}, \tag{64}$$

implying, in particular, energy relaxation equation (19),

$$\frac{dF_{\rm eff}}{dt}=-\int d^2x\left(\frac{\partial h}{\partial t}\right)^2<0. \tag{65}$$

Thus, $F_{\rm eff}$ generally decreases in time, and the interface goes into the ground state minimizing the effective free energy. By Eq. (63), $F_{\rm eff}$ is minimized only by minimizing both the local potential $U(\nabla h)>U_{\rm min}$ and the bending energy density $(\kappa/2)(\nabla^2 h)^2>0$. It follows that the interface ground state is flat (with zero bending energy), of the form $h(\mathbf{x})=\mathbf{M}_i\cdot\mathbf{x}$, where the slope $\mathbf{M}_i=\boldsymbol{\nabla} h$ minimizes the local potential $U(\mathbf{M})$. That is, $\mathbf{M}_i$ belongs to the energy minimum set $U(\mathbf{M}_i)=U_{\rm min}$, which is, in the presence of crystal anisotropy, a discrete set of Q points [see Figs. 2(b) and 2(c) for $Q=6$ and 4, respectively], whereas it degenerates into a circle in the absence of anisotropies [see Fig. 2(a)]. Formation of flat growing facets, with slopes $\mathbf{M}_i$, is thus naturally favored by the effective free-energy minimization. Even in the absence of crystal anisotropy, the interface breaks into growing facets and the edge networks form [see Secs. IV and VI]. This is further discussed here and in Appendix B.

Two facets, n and n', with slopes $\mathbf{M}_n$ and $\mathbf{M}_{n'}$, meet at a straight edge along the intersection of facets' planes $h_n=\mathbf{M}_n\cdot\mathbf{x}$ and $h_{n'}=\mathbf{M}_{n'}\cdot\mathbf{x}$. Commonly, both with and without anisotropy, all facets have the same slope magnitude, i.e., $|\mathbf{M}_n|=|\mathbf{M}_{n'}|=M_0$ (see Fig. 2). The edge formed by the facets n and n' is thus directed along the vector $\mathbf{M}_{\rm edge}=(\mathbf{M}_n+\mathbf{M}_{n'})/2$, which is, as well, the interface slope at a point on the edge. In particular, for $\mathbf{M}_n=-\mathbf{M}_{n'}$, the edge slope vanishes and one has a horizontal, ''roof-top'' edge. More generally, if 2ϕ is the angle between $\mathbf{M}_n$ and $\mathbf{M}_{n'}$, the edge slope magnitude $|\mathbf{M}_{\rm edge}|=M_0\cos(\phi)<M_0$. In discussing edges, it is convenient to go to the Cartesian coordinate system (x_1,x_2) with the x_1-axis perpendicular to the edge and the x_2-axis along the edge (see Appendix B). In this coordinate system, the facets' slopes are $\mathbf{M}_n=[-M_0\sin(\phi),M_0\cos(\phi)]$, $\mathbf{M}_{n'}=[M_0\sin(\phi),M_0\cos(\phi)]$, and thus, $h_n=-M_0\sin(\phi)x_1+M_0\cos(\phi)x_2$ and $h_{n'}=M_0\sin(\phi)x_1+M_0\cos(\phi)x_2$. The edge is the stationary solution of the equation of motion (64) that interpolates between the facets n and n': As discussed in Appendix B, for an edge, the interface profile is of the form

$$h(x_1,x_2)=M_0\sin(\phi)f(x_1)+M_0\cos(\phi)x_2. \tag{66}$$

Here $f(x_1)\approx|x_1|$ for $|x_1|\gg l_0=$the edge width, as discussed below and in the Appendix B. The associated slope field, $\mathbf{M}=\boldsymbol{\nabla} h$, thus has the form

$$\mathbf{M}(x_1,x_2)=[M_1(x_1),M_2]=[M_0\sin(\phi)f'(x_1),M_0\cos(\phi)]. \tag{67}$$

As $f'(x_1)\approx 1$ for $x_1\gg l_0$, and $f'(x_1)\approx -1$ for $x_1\ll -l_0$, $\mathbf{M}$ in Eq. (67) interpolates between the slopes of the facets n and n'.

As noted before in Sec. VI, edges carry extra costs of the effective free energy (in reference to the flat, infinite facet ground state), of the form

$$F_{\rm edge}=\sigma l_{\rm edge}, \tag{68}$$

where $l_{\rm edge}$ is the edge length (measured in the base plane, along the x_2 axis) whereas σ is the *edge line tension*. σ depends on the form of the local potential $U(\mathbf{M})$, as well as on which pair of facets is considered, as detailed in the following and in Appendix B. For the growth on isotropic surfaces, edge line tension is thus a continuous function of the angle between the facets' slope vectors$=2\phi$ [see, e.g., Eq. (72) below]. On the other side, in the presence of crystal anisotropy, there are Q energetically favored facet slope directions [see Figs. 2(b) and 2(c) for $Q=6$ and $Q=4$, respectively]. For each of $\binom{Q}{2}$ pairs of Q facets there is a distinct edge-type. For example, for the square anisotropy case depicted in Fig. 2(c), there are $Q=4$ degenerate energy minima, i.e., four types of facets, and, thus, six types of edges. Due to the discrete rotational symmetry, various edge types may have the same line tension. Generally, the line tension will depend on the angle 2ϕ between slope vectors of the facets forming the ridge. Thus, for the square anisotropy case depicted in Fig. 2(c), out of the six distinct edge types, four of them are formed by facet pairs with $2\phi=\pi/2$. These four types [identified before as ''regular edges,'' see Sec. VII] are related by 90-degree rotation and thus have a common value of the line tension. The remaining two types of edges are roof top edges, formed by facets pairs with $2\phi=\pi$. These two types of roof top edges are related by 90-degree rotation and thus have a common value of the line tension.

In the following, we will discuss edge line tension σ for various model forms of the local potential $U(\mathbf{M})$, both with and without anisotropies. Before proceeding, we elucidate another property of edges, namely the *edge surface current*. In contrast to infinite facets characterized by zero surface current, Eq. (2), edges carry a nonzero surface current running *along* them, see Appendix B. In the above-mentioned coordinate system, with x_1 perpendicular to the edge and x_2 along the edge, the current component perpendicular to the edge vanishes, $J_1=0$, whereas, as detailed in Appendix B,

$$J_2=J_2^{\rm NE}(M_1(x_1),M_2)=-\left.\frac{\partial U(M_1,M_2)}{\partial M_2}\right|_{M_1=M_1(x_1)}, \tag{69}$$

with $\mathbf{M}=[M_1(x_1),M_2]$ as in Eq. (67). As $\mathbf{M}$ approaches facet slopes for large x_1, the edge current J_2 in Eq. (69) is nonzero only within the edge width, $|x_1|<l_0$. Edges thus act as thin wires carrying surface currents. The net current flux flowing through an edge is

$$I_{\rm edge}=\int_{-\infty}^{+\infty}dx_1J_2=\int_{-\infty}^{+\infty}dx_1J_2^{\rm NE}(M_1(x_1),M_2). \tag{70}$$

Similar to edge line tension, edge current $I_{\rm edge}$ depends on the edge type. In particular, for roof top edges, this current is zero (as $M_2=0$).

Calculation of edge line tensions and edge currents is discussed in Appendix B. Here we quote results thus obtained for various model forms of the local potential. For example, for the isotropic potential of the form

$$U(\mathbf{M}) = -\frac{r}{2}(\mathbf{M})^2 + \frac{u}{4}[(\mathbf{M})^2]^2 = \frac{u}{4}[M_0^2 - (\mathbf{M})^2]^2 + \text{const}, \tag{71}$$

[with $M_0 = (r/u)^{1/2}$], used in the simulations of Sec. IV (see Appendix A), we find, for the edge tension,

$$\sigma(\phi) = \frac{2\sqrt{2}\kappa^{1/2} r^{3/2}}{3u} \sin^3(\phi); \tag{72}$$

as before, here 2ϕ = the angle between the slope vectors of the facets intersecting at the edge. The edge profile here is as in Eq. (66) with $f(x_1) = l_0 \ln[\cosh(x_1/l_0)]$, i.e., the interface slope is as in Eq. (67), with $f'(x_1) = \tanh(x_1/l_0)$. Here, l_0 is the edge width given by

$$l_0(\phi) = \frac{\sqrt{2}\kappa^{1/2}}{r^{1/2}} \frac{1}{\sin(\phi)}. \tag{73}$$

For the edge current, Eq. (70), we find, for $U(\mathbf{M})$ in Eq. (71),

$$I_{\text{edge}}(\phi) = \frac{2\sqrt{2}\kappa^{1/2} r}{u^{1/2}} \sin(\phi)\cos(\phi). \tag{74}$$

Note that the edge current in Eq. (74) is *uphill*, i.e., it has the same sign as the edge slope $M_2 = M_0 \cos(\phi)$. This is natural, as the interface slope at the edge $= M_0 \cos(\phi)$ is *smaller* than the preferred slope M_0 and the destabilizing effect dominates [see Fig. 1(c)]. Thus, by means of their uphill currents, the edges transport the material towards the pyramids' tops, thus contributing to the growth of pyramid heights.

Next, let us consider model local potentials $U(\mathbf{M})$ for the growth on square anisotropy surfaces such as the (001) surface. The simplest one, used in our simulations of Sec. VII (see Appendix A), has the form,

$$U(M_x, M_y) = -\frac{r}{2}[(M_x)^2 + (M_y)^2] + \frac{u}{4}[(M_x)^4 + (M_y)^4 + 2b(M_x)^2(M_y)^2], \tag{75}$$

or, in polar coordinates [$M_x = M\cos(\theta)$, $M_y = M\sin(\theta)$],

$$U(M, \theta) = -\frac{r}{2}M^2 + \frac{u(3+b)}{16}M^4 + \frac{u(1-b)}{16}M^4\cos(4\theta). \tag{76}$$

The local potential (75) generates the nonequilibrium current $J^{\text{NE}} = (J_x^{\text{NE}}, J_y^{\text{NE}})$, with

$$J_x^{\text{NE}} = -\frac{\partial U}{\partial M_x} = M_x[r - u(M_x)^2 - bu(M_y)^2],$$
$$J_y^{\text{NE}} = -\frac{\partial U}{\partial M_y} = M_y[r - u(M_y)^2 - bu(M_x)^2]. \tag{77}$$

Above, b is an anisotropy parameter; $b > -1$ to insure that the local potential (75) is bounded from below. For $b = +1$, the local potential (75), i.e., Eq. (76) depends only on the slope magnitude and reduces to the isotropic potential in Eq. (71), yielding the growth with the coarsening exponent $n_c = 1/3$ (see Sec. IV). For $b < 1$, local potential (75) has four minima at $[M_x, M_y] = [M_0\cos(\theta_n), M_0\sin(\theta_n)]$, with $M_0 = [2r/u(1+b)]^{1/2}$ and $\theta_n = 45° + (n-1)90°$, $n = 1$, 2, 3, and 4, as in Fig. 2(c). For $b = +1$, the energy minimum set *degenerates* into the circle with the radius $= M_0 = [r/u]^{1/2}$ [as in Fig. 2(a)] and one regains the isotropic potential (71). For $b > +1$, the model potential (75) is again anisotropic, however, with *new* locations of minima which are now at $[M_x, M_y] = [M_0\cos(\theta_n), M_0\sin(\theta_n)]$, with $M_0 = [r/u]^{1/2}$ and $\theta_n = (n-1)90°$, $n = 1$, 2, 3, and 4, i.e., the minima are now on coordinate axes. Thus, the facets that occur for $b > +1$ are rotated by 45° with respect to the facets that occur for $b < 1$. By tuning the anisotropy parameter b, one can go from the square anisotropy regime occurring for $b < +1$ to the other square anisotropy regime occurring for $b > +1$, by crossing the isotropic point $b = +1$. The four-sided pyramids and the edge networks that form for $b > +1$ are rotated by 45° with respect to those that form for $b < +1$. For example, for $b < +1$, the regular pyramid edges are parallel to the $x = 0$ and $y = 0$ axes (as in our simulation in Fig. 8), whereas for $b > +1$, the regular pyramid edges are parallel to the $x - y = 0$ and $x + y = 0$ axes.

Square anisotropy regimes we find for $b > 1$ and $b < 1$ (both characterized by the coarsening exponent $n_c = 1/4$, Secs. VII and VIII) are separated by the isotropic regime at $b = 1$, characterized by the coarsening exponent $n_c = 1/3$, as found in Sec. IV. Interestingly, such a sequence of interface transformations has been recently observed in more microscopic (kinetic Monte Carlo) simulations of Amar [23]. By tuning a microscopic model parameter, he was able to trigger a transition from the interface state as we described above to occur for $b < 1$, to another state, rotated by 45°, as we described above to occur for $b > 1$. Moreover, in the transition region between the two states, Amar finds a regime characterized by the ''isotropic exponent'' $n_c = 1/3$ and more complex patterns of edges [23]. These observations of [23] are strikingly similar to our findings above. We remark the facet orientations seen in [23] in the ''isotropic regime'' are certainly not random, as one would have in an isotropic potential, such as Eq. (76) for $b = 1$. Moreover, the observed ''isotropic regime'' exists over a *finite domain* in the parameter space [not just at a point, as the point $b = 1$ in the model (76)]. To explain these findings, we propose here a model generalizing Eq. (76) by inclusion of the *second harmonic* term,

$$U(M, \theta) = U_0(M) + U_1(M)\cos(4\theta) + U_2(M)\cos(8\theta). \tag{78}$$

The second harmonic term, U_2 in Eq. (78) is qualitatively important in situations in which the first harmonic term, U_1, goes to zero [e.g., at the isotropic point $b = 1$ in the model (76)]. With U_2 present, the true isotropic point is not accessible. To illustrate this, let us ignore the M dependence of U_1 and U_2 [by setting, simply, $U_1(M) = U_1(M_0)$ and $U_2(M) = U_2(M_0)$]. It is then easy to minimize Eq. (78) over the polar angle θ. This yields an interesting phase diagram depicted in Fig. 14 in the (U_1, U_2) plane. There we see *three* different phases of the system. Two of them we have already met before: Phase I, with four degenerate potential minima at

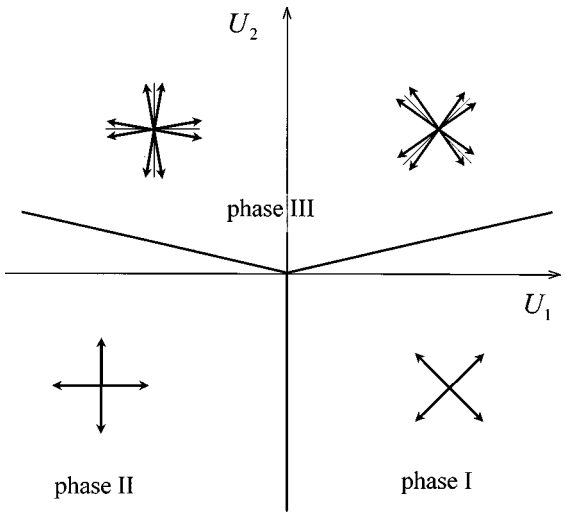

FIG. 14. Schematic phase diagram of the model in Eq. (78), in the (U_1, U_2) plane. We see three different phases of the system: (i) Phase I, with four degenerate energy minima at polar angles $\theta = 45° + (n-1)90°$, i.e., $\cos(4\theta) = -1$, (ii) phase II, with four minima at polar angles $\theta = (n-1)90°$, i.e., $\cos(4\theta) = +1$, and (iii) phase III, with *eight degenerate minima*, at the eight values of the polar angle solving the equation $\cos(4\theta) = -U_1/4U_2$. Phase III exists in the region $U_2 > |U_1|/4$. It is separated from phases I and II by a second-order phase transitions at which four minima of these phases *bifurcate* into eight minima of phase III. For $U_2 > 0$, phase III intervenes between phases I and II, and facet orientations vary continuously throughout phase III from those of the phase I to those of the phase II. On the other side, for $U_2 < 0$, by changing U_1, one can directly go from phase I to the phase II, by crossing first-order phase transition at the point $U_1 = 0$, at which there is abrupt 45-degree rotation of facet orientations from those of the phase I to those of the phase II.

polar angles $\theta_n = 45° + (n-1)90°$, i.e., $\cos(4\theta) = -1$, and Phase II, with four minima at polar angles $\theta_n = (n-1)90°$, i.e., $\cos(4\theta) = +1$. These phases occur already within the single harmonic model (76). In addition to them, due to the presence of the second harmonic term in our model (78), there is a novel phase, referred to as Phase III in Fig. 14. It is characterized by the presence of *eight degenerate energy minima*, at the eight values of the polar angle θ solving the equation

$$\cos(4\theta) = -\frac{U_1}{4U_2}. \tag{79}$$

Phase III exists in the region $U_2 > |U_1|/4$, see Fig. 14. Phase III is separated from the phases I and II by second-order phase transitions. At these transitions, four minima of phases I and II continuously *bifurcate* into the eight minima of phase III. For $U_2 > 0$, by changing U_1, one can go from Phase I to phase II *only* by passing through phase III, see Fig. 14. On the other side, for $U_2 < 0$, by changing U_1, one can directly go from phase I to phase II, by crossing the first-order phase transition at the point $U_1 = 0$, at which four potential minima of phase I coexist with four potential minima of phase II. Across this transition, there is an abrupt 45-degree rotation of facet orientations from those of phase I to those of phase II. In contrast to this, for $U_2 > 0$, phase III intervenes between phases I and II, and facet orientations [obtained by Eq. (79)] vary continuously throughout phase III, from those of phase I to those of phase II (as indicated in Fig. 14). Remarkably, phase III has eight degenerate energy minima, i.e., eight possible types of facets in comparison to only four types that occur in phases I and II. Within phase III, the interface may exhibit the isotropic coarsening exponent $n_c = 1/3$, as suggested by our simulations of the systems with large number of allowed facets types occurring in the growth on (111) surfaces [see Secs. V and VI]. While this point needs to be explored in future work, it suggests that phase III may well correspond to the interface state found to exhibit the isotropic coarsening exponent $n_c = 1/3$ in Ref. [23]. The particular location that we find in Fig. 14 for Phase III, as an intervening phase between phase I and phase II (both with $n_c = 1/4$), directly corresponds the observations of Ref. [23]. The fact that our phases I and II are directly related to those seen in Ref. [23] (they are mutually related by 45-degree rotation, etc.), simply indicates that the phenomena observed in that work are related to a change of sign of the first harmonic term U_1. This directly leads to our phenomenological model in Eq. (78), which predicts the intervening Phase III as a natural candidate for the interface state found to exhibit the isotropic coarsening exponent $n_c = 1/3$ in Ref. [23]. On the other hand, an alternative interpretation for the findings of Ref. [23] is that the regime with $n_c = 1/3$ corresponds to the first-order transition between phases I and II that occurs for $U_2 < 0$ at $U_1 = 0$, see Fig. 14. Precisely at the phase-transition point, the local potential (78) has eight degenerate minima at $\theta_n = (n-1)45°$ ($n = 1$ to 8) forming a regular octagon in the **M** space. At this transition, the interface would look like a mixture of phases I and II, similar to findings of Ref. [23]. We stress, however, that reaching this transition point may require a fine tuning of the system's parameters. For example, within the model (78) U_1 has to be set to zero as only then all eight minima have the same energy. Still, for a small U_1, the U_2 term in Eq. (78) may dominate at short-time scales. Under this condition, during the early stage of evolution the interface would appear as a mixture of phases I and II.

We proceed by a discussion of edges in the simplest model with square anisotropy in Eq. (75). As noted above, here we expect two kinds of edges: (i) regular edges formed by facet pairs with $2\phi = \pi/2$, and (ii) roof top edges, formed by facets pairs with $2\phi = \pi$. (2ϕ is the angle between slope vectors of the two facets intersecting at the edge.) For example, in Fig. 2(c) regular edges are formed by facets pairs (n, n'), with slopes $\mathbf{M}_n$ and $\mathbf{M}_{n'}$, for $(n, n') = (1,2)$, (2, 3),(3, 4), and (4, 1), whereas roof top edges are formed by the facet pairs $(n, n') = (1,3)$ and (2, 4). Edge line tensions σ and edge currents I_{edge} are model dependent as detailed in Appendix B. Consider, for example the local potential in Eq. (75), with the anisotropy parameter $b < 1$ (then the potential minima are at $\theta_n = 45° + (n-1) \cdot 90°$, $n = 1$, 2, 3, and 4, as in Fig. 2(c). We find, for the line tension of the regular edges $(2\phi = \pi/2)$,

$$\sigma_{\text{reg}} = \frac{2\sqrt{2}\,\kappa^{1/2} r^{3/2}}{3(1+b)^{3/2} u}, \quad b < 1, \tag{80}$$

whereas their surface current is

$$I_{\rm reg}=\frac{2\sqrt{2}b\kappa^{1/2}r}{(1+b)u},\quad b<1. \tag{81}$$

The regular edge profile here is as in Eq. (66) with $M_0=[2r/u(1+b)]^{1/2}$, $2\phi=\pi/2$, and $f(x_1)=l_{\rm reg}\ln[\cosh(x_1/l_{\rm reg})]$, i.e., the interface slope is as in Eq. (67), $[M_1(x_1),M_2]=[M_0\sin(\phi)f'(x_1),M_0\cos(\phi)]$, with $f'(x_1)=\tanh(x_1/l_{\rm reg})$. Here, $l_{\rm reg}$ is the regular edge width given by

$$l_{\rm reg}=\frac{\sqrt{2}(1+b)^{1/2}\kappa^{1/2}}{r^{1/2}},\quad b<1. \tag{82}$$

Next, we proceed to discuss the *roof-top* edges for $b<1$. We find, for their line tension,

$$\sigma_{\rm rt}=\frac{4\sqrt{2}\kappa^{1/2}r^{3/2}}{3(1+b)u},\quad b<1, \tag{83}$$

whereas their surface current is zero,

$$I_{\rm rt}=0. \tag{84}$$

In the coordinate system associated with the roof top edge (with the x_2 axis along and the x_1 axis perpendicular to the edge), its profile here is as in Eq. (66) with $M_0=[2r/u(1+b)]^{1/2}$, $2\phi=\pi$, and $f(x_1)=l_{\rm rt}\ln[\cosh(x_1/l_{\rm rt})]$, i.e., the interface slope is as in Eq. (67), $[M_1(x_1),M_2]=[M_0\sin(\phi)f'(x_1),M_0\cos(\phi)]=[M_0f'(x_1),0]$, with $f'(x_1)=\tanh(x_1/l_{\rm rt})$. Here, $l_{\rm rt}$ is the roof top edge width given by

$$l_{\rm rt}=\frac{\sqrt{2}\kappa^{1/2}}{r^{1/2}}. \tag{85}$$

Using Eqs. (80) and (83), the ratio of the line tensions of rooftop and regular edges is

$$\frac{\sigma_{\rm rt}}{\sigma_{\rm reg}}=2\sqrt{1+b},\quad b<1. \tag{86}$$

As indicated above, Eqs. (80)–(83), and Eq. (86), apply for the case $b<1$, when the potential minima are at polar angles $\theta_n=45°+(n-1)\cdot 90°$, $n=1$, 2, 3, and 4, as in Fig. 2(c). As discussed before, for $b>1$, the local potential minima are at $\theta_n=(n-1)\cdot 90°$, $n=1$, 2, 3, and 4, and, in effect, four-sided pyramids and the edge networks that form for $b>+1$ are rotated by 45° with respect to those that form for $b<+1$. Formulas for the edge energies, currents, etc., for the case $b>1$, can be obtained from the above formulas for $b<1$, by using the following mathematical property of Eq. (75): A 45-degree base plane rotation maps the potential (75) into itself with, however, changed parameters. By this rotation, $[b,u]\rightarrow[b',u']$, where

$$b'=\frac{3-b}{1+b}, \tag{87}$$

$$u'=\frac{1+b}{2}u. \tag{88}$$

By a 45-degree rotation, a potential with $b>1$ maps into a potential with $b'<1$ [as can be seen by noting that Eq. (87) is equivalent to $(1+b)(1+b')=4$]. Due to this, it is enough to study the model (75), analytically or by numerical simulations, just in the range $b<1$. In particular, formulas for edge tensions, currents, and widths that apply for $b>1$, can be obtained from the above corresponding formulas that apply for $b<1$, by replacing $[b,u]$ therein with $[b'=(3-b)/(1+b),\ u'=(1+b)u/2]$. By using this, we find, for the line tension of the regular edges,

$$\sigma_{\rm reg}=\frac{(1+b)^{1/2}\kappa^{1/2}r^{3/2}}{3\sqrt{2}u},\quad b>1. \tag{89}$$

Their surface current is

$$I_{\rm reg}=\frac{\sqrt{2}(3-b)\kappa^{1/2}r}{(1+b)u},\quad b>1. \tag{90}$$

Regular edge width is given by

$$l_{\rm reg}=\frac{2\sqrt{2}\kappa^{1/2}}{(1+b)^{1/2}r^{1/2}},\quad b>1. \tag{91}$$

By the same replacement, we find, for the line tension of roof-top edges,

$$\sigma_{\rm rt}=\frac{2\sqrt{2}\kappa^{1/2}r^{3/2}}{3u},\quad b>1, \tag{92}$$

The roof-top edge surface current ($=0$) and the width are given by Eqs. (84) and (85) for any b. Using Eqs. (89) and (92), the ratio of the line tensions of rooftop and regular edges is

$$\frac{\sigma_{\rm rt}}{\sigma_{\rm reg}}=\frac{4}{\sqrt{1+b}},\quad b>1. \tag{93}$$

We proceed by discussing some features of the above results. First, note that the regular edge current is positive (''uphill'') only for $0<b<3$, see Eqs. (81) and (90). On the other side, for $b<0$ or $b>3$, the edge current is negative, *downhill*. As noted before [see the discussion following Eq. (74)], as the interface slope at the edge$=M_0\cos(\phi)$ is *smaller* than the preferred slope M_0, it would be natural to expect a *positive* edge current in a realistic MBE growth model [the destabilizing Schwoebel-Ehrlich effect should then dominate, see Fig. 1(c)]. It is thus unlikely that the model in Eqs. (75)–(77) with $b<0$, or $b>3$, is of a more direct physical interest. For this reason, we have focused our simulations on the anisotropy parameter range $0<b<3$. Moreover, using Eq. (87), models with $3>b>1$ can be mapped into models with $0<b<1$. It is thus sufficient to restrict our study to the range $0<b<1$. With these observations in mind, we carried the simulations of Sec. VII by choosing $b=1/2$.

For $0<b<3$, regular pyramid edges have uphill currents transporting material towards the pyramids' tops, thus contributing to the growth of pyramid heights. On the other side, for $-1<b<0$, or for $b>3$, regular pyramid ridges have downhill currents. Though, as noted above, such a situation may not correspond to realistic MBE growth, it may be interesting in its own right. In relation to this, we comment on a recent work of Siegert [22], who numerically investigated the range $b<0$. He claims observing a special value of b (he estimates to be $b_c^{\rm Siegert}=-3/4$), such that a coarsening with

$n_c=1/3$ occurs at b_c, whereas for $b>b_c$ one has the coarsening with $n_c=1/4$. It was suggested in [22], that, at b_c, the line tensions of rooftop and regular ridges are related by $\sigma_{\rm reg}=\sqrt{2}\sigma_{\rm rt}$. By combining this relation with our result in Eq. (86), we find $b_c=-7/8$. This is smaller than the value $b_c^{\rm Siegert}=-3/4$, as our correct edge line tensions in Eqs. (80) and (83) differ from those used in Ref. [22]. Thus, the fact that the data of Ref. [22] suggest coarsening with $n_c=1/3$ already at $b=-3/4$ needs to be understood.

Having said this, we reiterate our skepticism in reference to physical relevance of the simple model (75) outside the range $0<b<3$. Having, in this model, a coarsening with $n_c=1/3$, somewhere outside the range $0<b<3$, is unlikely to have some significance in explaining seemingly similar observations from experiments and realistic kinetic Monte Carlo simulations on square anisotropy (001) surfaces. Though, to our knowledge, no experiment, thus far, has suggested such a coarsening, recent simulations of Amar [23] offer a realistic possibility of having a regime with $n_c=1/3$ coarsening on (001) surfaces. As detailed before in this section, understanding of this regime requires going beyond the simple model (75) to more general models, such as the one we proposed in Eq. (78).

X. SUMMARY

The growth on isotropic and hexagonal symmetry (111) surfaces was shown to exhibit a scaling behavior characterized by the presence of a single characteristic length scale $\lambda(t)$=pyramid size that grows in time as a power law. Our numerical simulations suggest that the growth of the characteristic length scale is governed by the same coarsening exponents for both isotropic and hexagonal symmetry (111) surfaces. The coarsening exponent obtained is $n_c\cong 0.33$. The kinetic scaling theory that explains this scaling behavior was presented in this work in Sec. VI. It employs the fact that the effective free energy of growing interfaces is localized within edge networks. These networks form across the interface, both with and without spatial anisotropy present.

The growth on the square symmetry (001) surfaces is more subtle. In this case, pyramid edges form nearly perfect square lattices disordered by irregularly placed dislocations. The interfacial coarsening is mediated by motion of the dislocations that we characterized here as the dislocation climb. The presence of the dislocations is thus crucial for the coarsening of the square symmetry (001) surfaces. In fact, in numerical simulations, the coarsening essentially stops as soon as the average distance between the dislocations reaches the size of the system that is simulated. The growth on the square symmetry (001) surfaces exhibits a multiscaling behavior, as there are two characteristic length scales that grow in time with two different coarsening exponents. One of them is the pyramid lateral size$\sim$pyramid height, growing with the coarsening exponent $n_c\cong\beta\cong 0.25$. The other length scale $\xi(t)$, the distance between the dislocations in the same row of the edge lattice, grows faster with a different exponent $n_\xi\cong 0.50$. Kinetic scaling theory that explains the coarsening exponents for the square symmetry (001) surfaces was presented in this work in Sec. VIII. The theory shows that the dislocation climb and dislocation annihilation processes going on across the edge network are essential for understanding of the coarsening dynamics on this type of surfaces. Other possible dislocation processes, such as the dislocation-pair production, or occasional formations of unstable bound states between two dislocations moving in different directions (one vertically, the other one horizontally; see, e.g., Fig. 19 in Appendix C), insignificantly affect the coarsening. In fact, a significant dislocation production occurs only during the initial (precoarsening) stage of the growth. Subsequently, production of new dislocations is energetically hindered, as it would introduce new pyramid edges and cause an increase of the effective free energy. The coarsening on the square symmetry (001) surfaces is, generally, an extinction of pyramid edges and facets mediated by climbing dislocations. Rate of this extinction crucially depends on the number of dislocations present across the interface. During the late time film evolution (i.e., coarsening), total number of dislocations decreases in time due to their annihilations with other dislocations (or with the film lateral boundaries). These effects are incorporated into our kinetic scaling theory that is used in Sec. VIII to analytically explain coarsening exponents observed in experiments and previous numerical simulations of the growth on (001) surfaces.

Finally, we note that the interface growth phenomena discussed in this paper are similar to the buckling dynamics of elastic manifolds (elastic rods and tethered membranes) investigated in our recent works [24,25].

ACKNOWLEDGMENTS

We thank Mylan Laboratories and the NSF WV EPSCoR program for support. Numerical simulations were performed on the CM-5 parallel computer of the West Virginia University.

APPENDIX A

In this Appendix, we give a detailed description of our modeling scheme. First, we describe how we solve the type-*A* evolution equation (4) for the MBE growth on a hexagonal (i.e., equilateral triangle) grid. Such a grid is natural for simulating the growth on hexagonal symmetry surfaces. With each node of the hexagonal grid, with the location $\mathbf{x}=(x_1,x_2)$ in the base plane, we associate the interface height $h(\mathbf{x})$. Further, we associate with the height configuration $\{h\}$, a suitable defined effective free energy $F_{\rm eff}(\{h\})$ (see below), and simply integrate the type-*A* dynamics equations

$$\frac{dh(\mathbf{x})}{dt}=-\frac{\partial F_{\rm eff}}{\partial h(\mathbf{x})}$$

with a discretized time.

We proceed by discussing the discrete form of the two terms of the effective free energy $F_{\rm eff}$ [see Eq. (5)]. The first, surface diffusion term (''bending energy'') is defined on the hexagonal grid in the following way:

$$F_{\rm SD}=\frac{\kappa}{2}\sum_{\mathbf{x}}\left\{\frac{\sum_{j=1}^{3}[h(\mathbf{x}+\mathbf{a}_j)+h(\mathbf{x}-\mathbf{a}_j)]}{6}-h(\mathbf{x})\right\}^2. \tag{A1}$$

Here, $\pm\mathbf{a}_j$, $j=1,2,3$, are the nearest-neighbor bond vectors of the hexagonal grid. In the continuum limit, the expression in Eq. (A1) yields the expression (6) for the bending energy:

$$F_{\mathrm{SD}} \sim \int d^2x (\nabla^2 h)^2 + \cdots, \tag{A2}$$

where the ellipses indicate the terms with higher-order derivatives of $h(\mathbf{x})$. To model the local potential term in Eq. (5), we consider F_{NE} in the form

$$F_{\mathrm{NE}} = \sum_{\mathbf{x}} \left\{ \sum_{j=1}^{3} \Phi[h(\mathbf{x}+\mathbf{a}_j) - h(\mathbf{x})] \right\}, \tag{A3}$$

where the function $\Phi(\Delta h)$ has the property $\Phi(\Delta h) = \Phi(-\Delta h)$ and we are free to choose it. In the continuum limit we have

$$F_{\mathrm{NE}} \sim \int d^2x U(\nabla h) + \text{higher derivative terms}, \tag{A4}$$

with

$$\begin{aligned} U(\mathbf{M}) &= \Phi(\mathbf{M}\cdot\mathbf{a}_1) + \Phi(\mathbf{M}\cdot\mathbf{a}_2) + \Phi(\mathbf{M}\cdot\mathbf{a}_3) \\ &= \Phi(|\mathbf{M}|\cos(\theta)) + \Phi\left(|\mathbf{M}|\cos\left(\theta - \frac{2\pi}{6}\right)\right) \\ &\quad + \Phi\left(|\mathbf{M}|\cos\left(\theta - \frac{4\pi}{6}\right)\right). \end{aligned} \tag{A5}$$

Resulting nonequilibrium current is of the form

$$\begin{aligned} \mathbf{J}_{\mathrm{NE}} &= -\frac{\partial U(\mathbf{M})}{\partial \mathbf{M}} \\ &= -\Phi'(\mathbf{M}\cdot\mathbf{a}_1)\mathbf{a}_1 - \Phi'(\mathbf{M}\cdot\mathbf{a}_2)\mathbf{a}_2 - \Phi'(\mathbf{M}\cdot\mathbf{a}_3)\mathbf{a}_3. \end{aligned} \tag{A6}$$

The expression for the local potential, Eq. (A5) can be reexpressed as the Fourier series

$$\begin{aligned} U(|\mathbf{M}|,\theta) &= U\left(|\mathbf{M}|,\theta+\frac{2\pi}{6}\right) \\ &= U_0(|\mathbf{M}|) + 2\sum_{n=1}^{\infty} U_n(|\mathbf{M}|)\cos(6n\pi), \end{aligned}$$

$$U_n(|\mathbf{M}|) = 3\int_{-\pi}^{+\pi} \frac{d\theta}{2\pi} \Phi(|\mathbf{M}|\cos\theta)\cos(6n\theta). \tag{A7}$$

For example, if we use for the function $\Phi(\Delta h)$ the following expression:

$$\Phi(\Delta h) = a_0 + a_2(\Delta h)^2 + a_4(\Delta h)^4 + a_6(\Delta h)^6, \tag{A8}$$

then, by Eq. (A7),

$$U(|\mathbf{M}|,\theta) = U_0(|\mathbf{M}|) + 2U_1(|\mathbf{M}|)\cos(6\theta), \tag{A9}$$

whereas all higher-order harmonics vanish $[0 = U_2(|\mathbf{M}|) = U_3(|\mathbf{M}|) = \ldots]$. In Eq. (A9), the coefficients $U_0(|\mathbf{M}|)$ and $U_1(|\mathbf{M}|)$ are

$$U_0(|\mathbf{M}|) = 3a_0 + \frac{3}{2}a_2|\mathbf{M}|^2 + \frac{9}{8}a_4|\mathbf{M}|^4 + \frac{15}{16}a_6|\mathbf{M}|^6, \tag{A10}$$

and

$$U_1(|\mathbf{M}|) = \frac{3}{64}a_6|\mathbf{M}|^6. \tag{A11}$$

Already from the last two equations, we can see that there are two interesting situations to study [notice that $U_1(|\mathbf{M}|)$ depends only on a_6 and, moreover, vanishes for $a_6 = 0$]:

Case $a_6 > 0$: Using the

$$\mathbf{J}_{\mathrm{NE}} = -\frac{\partial U(\mathbf{M})}{\partial \mathbf{M}}$$

we get six local potential minima with vanishing $\mathbf{J}_{\mathrm{NE}}$, that is

$$\mathbf{J}_{\mathrm{NE}} = 0 \text{ at } \begin{cases} \theta = \dfrac{\pi}{6} + n\dfrac{2\pi}{6}, \quad n = 0,1,2,3,4,5 \\ |\mathbf{M}| = M_0 \end{cases}, \tag{A12}$$

where M_0 is the value of $|\mathbf{M}|$ minimizing $U(|\mathbf{M}|, \theta = \pi/6)$. This corresponds to the hexagonal symmetry surfaces, see Fig. 2(b).

Case $a_6 = 0$: This gives $\mathbf{J}_{\mathrm{NE}} = 0$ along a circle $|\mathbf{M}| = M_0$ in the order-parameter space, due to the fact that $U(\mathbf{M})$ does not depend on the polar angle θ [see Eqs. (A9) and (A11)]. This case can be thus used to model the growth in the *absence* of surface anisotropy, see Fig. 2(a).

Equation (A8) can be conveniently rewritten as

$$\Phi(\Delta h) = \frac{b_1}{2}e^2 + \frac{b_2}{3}e^3 + \text{const}, \tag{A13}$$

where e is given by

$$e = \frac{(\Delta h)^2 - (\Delta h_0)^2}{2}. \tag{A14}$$

b_1, b_2, and Δh_0 are numerical constants simply related to those in Eq. (A8). In our simulations we set $(\Delta h_0)^2 = 0.2$ and modified only the coefficients b_1 and b_2. By Eqs. (A8) and (A13), $a_6 = b_2/24$. According to the above discussion, the choice $b_2 = 0$ thus generates a local potential which is rotationally invariant. We remark though that higher derivative terms indicated in Eqs. (A2) and (A4) break the perfect rotational symmetry. Nonetheless, with $b_2 = 0$, the rotational invariance is exact for *flat* interface configurations. Thus, even for the discretized model, one has the circular continuum set of degenerate energy minima in Fig. 2(a) corresponding to flat interfaces with the slope vector $\mathbf{M} = \nabla h$ having a fixed magnitude M_0 and arbitrary direction. This method (of choosing $b_2 = 0$) on the hexagonal discrete grid, was one of the methods we used to simulate the growth on isotropic surfaces. The other method we used was to use a square discrete grid and an appropriate form of the local potential, as discussed later on [see Eq. (A25)].

Finally, we give description of our modeling scheme for square symmetry surfaces. Here, we solved the evolution equation (4) for the MBE growth on a square grid. As for the hexagonal case, with each node of this grid, with the location

$\mathbf{x}=(x_1,x_2)$ in the base plane, we associate the interface height $h(\mathbf{x})$. Further, we associate, with the height configuration $\{h\}$, a suitable defined effective free energy $F_{\rm eff}(\{h\})$ (see below), and simply integrate the type-*A* dynamics equations:

$$\frac{dh(\mathbf{x})}{dt}=-\frac{\partial F_{\rm eff}}{\partial h(\mathbf{x})}$$

with a discretized time.

We proceed by describing the discrete form of the two terms of the effective free-energy $F_{\rm eff}$ [see Eq. (5)]. The first, surface diffusion term (''bending energy'') is defined on the square grid in the following way:

$$F_{\rm SD}=\frac{\kappa}{2}\sum_{\mathbf{x}}\left\{\frac{\sum_{j=1}^{2}[h(\mathbf{x}+\mathbf{a}_j)+h(\mathbf{x}-\mathbf{a}_j)]}{4}-h(\mathbf{x})\right\}^2. \tag{A15}$$

Here, $\pm\mathbf{a}_j$, $j=1,2$, are the nearest-neighbor bond vectors of the square grid. In the continuum limit, the expression in Eq. (A15) yields the expression (6) for the bending energy:

$$F_{\rm SD}\sim\int d^2x(\nabla^2h)^2+\cdots, \tag{A16}$$

where the ellipses indicate the terms with higher-order derivatives of $h(\mathbf{x})$. To model the local potential term in Eq. (5), we consider $F_{\rm NE}$ in the form

$$\begin{aligned}F_{\rm NE}=\sum_{\mathbf{x}}\Big\{&\Phi_{\rm nnn}[h(\mathbf{x}+\mathbf{a}_2+\mathbf{a}_1)-h(\mathbf{x})]\\&+\Phi_{\rm nnn}[h(\mathbf{x}+\mathbf{a}_2-\mathbf{a}_1)-h(\mathbf{x})]\\&+\sum_{j=1}^{2}\Phi_{\rm nn}[h(\mathbf{x}+\mathbf{a}_j)-h(\mathbf{x})]\Big\},\end{aligned} \tag{A17}$$

where the functions $\Phi_{\rm nnn}(\Delta h)$ (the next-nearest-neighbor term) and $\Phi_{\rm nn}(\Delta h)$ (the nearest-neighbor term) have the properties $\Phi_{\rm nnn}(\Delta h)=\Phi_{\rm nnn}(-\Delta h)$ and $\Phi_{\rm nn}(\Delta h)=\Phi_{\rm nn}(-\Delta h)$ and we are free to choose them. In the continuum limit we have

$$F_{\rm NE}\sim\int d^2xU(\nabla h)+\text{higher derivative terms}, \tag{A18}$$

with

$$\begin{aligned}U(\mathbf{M})=&\Phi_{\rm nnn}(M_1+M_2)+\Phi_{\rm nnn}(M_2-M_1)+\Phi_{\rm nn}(M_1)\\&+\Phi_{\rm nn}(M_2).\end{aligned} \tag{A19}$$

We used in Eq. (A17) the following forms for the functions $\Phi_{\rm nnn}(\Delta h)$ and $\Phi_{\rm nn}(\Delta h)$:

$$\Phi_{\rm nnn}(\Delta h)=\frac{c_2}{16}(\Delta h)^4, \tag{A20}$$

$$\Phi_{\rm nn}(\Delta h)=\frac{c_1}{2}e^2, \tag{A21}$$

$$e=\frac{(\Delta h)^2-(\Delta h_0)^2}{2}, \tag{A22}$$

where c_1, c_2, and Δh_0 are constants that allow us to choose various shapes for the local potentials and, therefore, various shapes for the nnequilibrium current, corresponding to square symmetry surfaces. In our simulations we fixed $(\Delta h_0)^2=0.2$ and we modified only the coefficients c_1 and c_2. By Eqs. (A19)–(A22), the local potential has the form

$$\begin{aligned}U(\mathbf{M})=&\frac{c_2}{16}[(M_1+M_2)^4+(M_1-M_2)^4]\\&+\frac{c_1}{8}[(M_1^2-(\Delta h_0)^2)^2+(M_2^2-(\Delta h_0)^2)^2].\end{aligned} \tag{A23}$$

Equation (A23) can be conveniently rewritten as

$$U(\mathbf{M})=-\frac{r}{2}(M_1^2+M_2^2)+\frac{u}{4}(M_1^4+M_2^4+2bM_1^2M_2^2)+\text{const}, \tag{A24}$$

or, in polar coordinates $[M_1=M\cos\theta,\ M_2=M\sin\theta]$, as

$$U(\mathbf{M})=-\frac{r}{2}M^2+\frac{u(3+b)}{16}M^4+\frac{u(1-b)}{16}M^4\cos(4\theta), \tag{A25}$$

with

$$r=\frac{c_1(\Delta h_0)^2}{2},\ u=\frac{c_1+c_2}{2},\ \text{and}\ \ b=\frac{3c_2}{c_1+c_2}.$$

Local potential in Eqs. (A24) and (A25) is discussed in more detail in Sec. IX. Using Eq. (A25) we see that this potential becomes isotropic for $b=1$ and can be thus used to numerically simulate the growth on isotropic surfaces. We used this to check our findings on isotropic surfaces obtained by using the hexagonal grid, as described before in this Appendix (see the case $a_6=b_2/24=0$). Eventually, we have found that properties of interface morphologies (edge network) as well as the coarsening exponent $n_c=1/3$, obtained by these two markedly different approaches to isotropic surfaces, are the same.

APPENDIX B

Here we outline the calculation of edge line tensions and edge currents discussed in Sec. IX. Edges are stationary solutions of the interface equation of motion (4),

$$\frac{\partial h(x,t)}{\partial t}=-\frac{\Delta F_{\rm eff}}{\delta h(x,t)}, \tag{B1}$$

where $F_{\rm eff}$ is the effective free energy

$$\begin{aligned}F_{\rm eff}&=\int d^2x\left[U(\boldsymbol{\nabla}h)+\frac{\kappa}{2}(\nabla^2h)^2\right]\\&=\int d^2x\left[U(\mathbf{M})+\frac{\kappa}{2}(\boldsymbol{\nabla}\cdot\mathbf{M})^2\right];\end{aligned} \tag{B2}$$

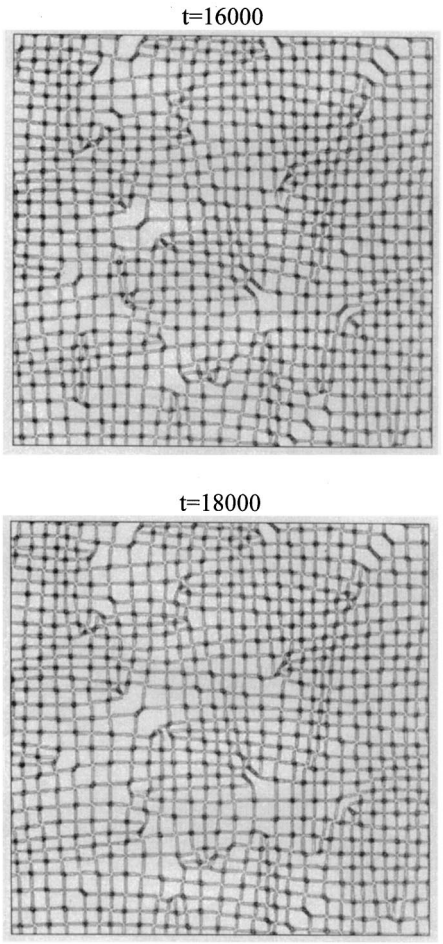

FIG. 15. A small portion (300×300) of the network of edges for the square anisotropy surfaces at times $t=16\,000$ and $t=18\,000$.

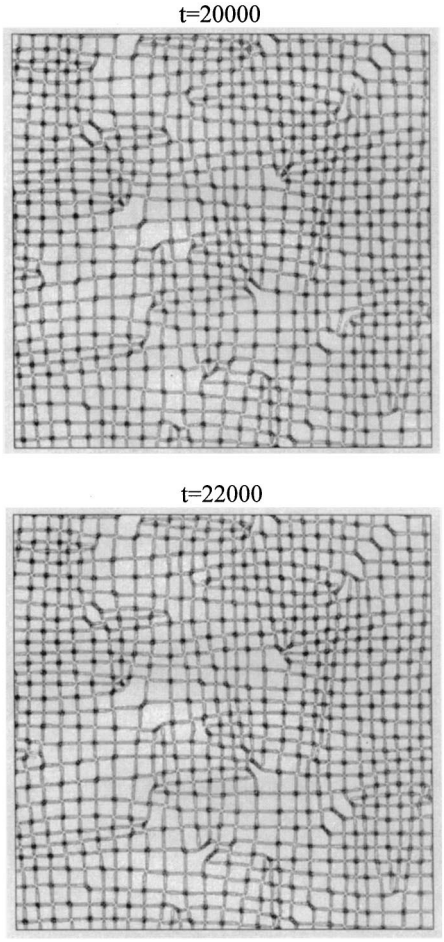

FIG. 16. The same as in Fig. 15, here at times $t=20\,000$ and $t=22\,000$.

here $\mathbf{M}=\boldsymbol{\nabla}h$ is the interface slope. As noted in Sec. III, Eq. (B1) is equivalent to

$$\frac{\partial h}{\partial t}=-\boldsymbol{\nabla}\cdot\mathbf{J}, \tag{B3}$$

where $\mathbf{J}$ is the surface current,

$$\mathbf{J}=\mathbf{J}_{\mathrm{NE}}(\mathbf{M})+\kappa\boldsymbol{\nabla}(\nabla^2 h)=\mathbf{J}_{\mathrm{NE}}(\mathbf{M})+\kappa\nabla^2\mathbf{M}. \tag{B4}$$

Here, $\mathbf{J}_{\mathrm{NE}}(\mathbf{M})$ is the nonequilibrium surface current, related to the local potential $U(\mathbf{M})$ by

$$\mathbf{J}_{\mathrm{NE}}(\mathbf{M})=-\frac{\partial U}{\partial\mathbf{M}}. \tag{B5}$$

Edges are stationary solutions of Eq. (B3), i.e., $\partial h/\partial t=0$. For them, with Eq. (B3), $\boldsymbol{\nabla}\cdot\mathbf{J}=0$, i.e.,

$$\frac{\partial J_1}{\partial x_1}+\frac{\partial J_2}{\partial x_2}=0. \tag{B6}$$

Using Eqs. (B4) and (B5),

$$J_1=-\frac{\partial U(M_1,M_2)}{\partial M_1}+\kappa\nabla^2 M_1,$$

$$J_2=-\frac{\partial U(M_1,M_2)}{\partial M_2}+\kappa\nabla^2 M_2; \tag{B7}$$

here $M_i=\partial h(x_1,x_2)/\partial x_i$, $i=1,2$. To obtain the edge profile, we seek a solution of Eq. (B6) of the form

$$h(x_1,x_2)=\Psi(x_1)+\alpha\cdot x_2, \tag{B8}$$

where α is a constant and $\Psi(x_1)$ is a function of x_1 only, yet to be determined. With $h(x_1,x_2)$ as in Eq. (B8), the interface slope, $\mathbf{M}=\boldsymbol{\nabla}h$ has the form

$$M_1=\Psi'(x_1),\quad M_2=\alpha, \tag{B9}$$

i.e., M_1 is a function of x_1 only, whereas M_2 is just a constant. Using Eqs. (B9) and (B7),

$$J_1=-\left.\frac{\partial U(M_1,M_2)}{\partial M_1}\right|_{\substack{M_1=M_1(x_1)\\M_2=\alpha}}+\kappa\frac{d^2M_1}{dx_1^2}, \tag{B10}$$

$$J_2=J_2^{NE}(M_1(x_1),\alpha)=-\left.\frac{\partial U(M_1,M_2)}{\partial M_2}\right|_{\substack{M_1=M_1(x_1)\\M_2=\alpha}}. \tag{B11}$$

Note that the above J_1 and J_2 are functions of x_1 only. Thus, Eq. (B6) reduces to

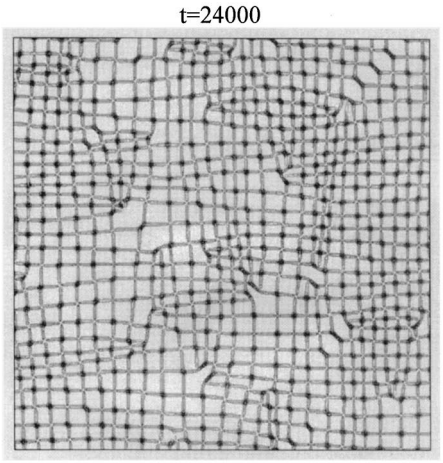

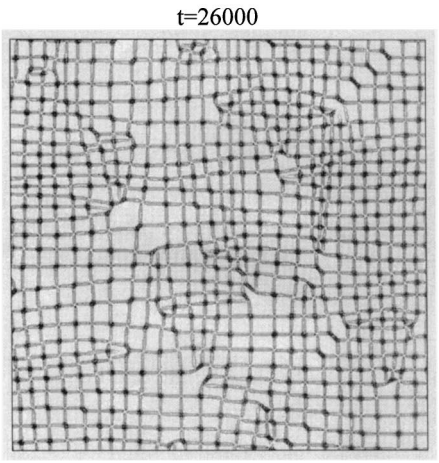

FIG. 17. The same as in Fig. 15, here at times $t=24\,000$ and $t=26\,000$.

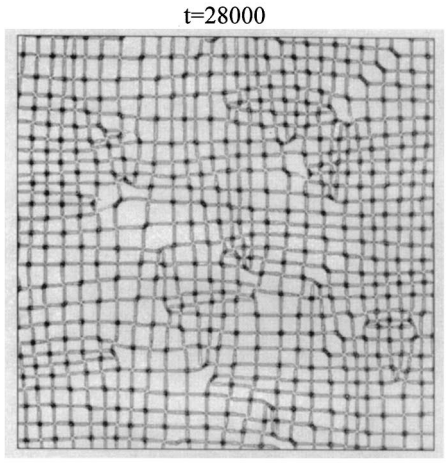

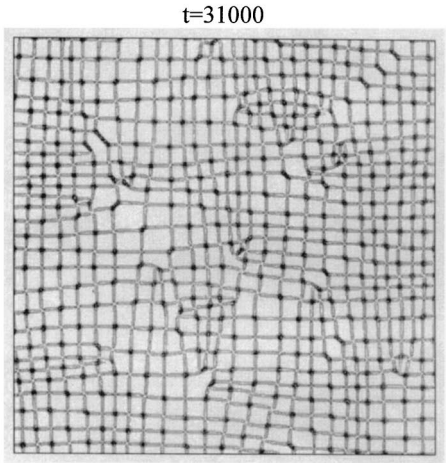

FIG. 18. The same as in Fig. 15, here at times $t=28\,000$ and $t=31\,000$.

$$\frac{dJ_1}{dx_1}=0. \tag{B12}$$

Thus, J_1 must be a constant. This constant must be zero for edge solutions. Indeed, for a single long edge, the surface current must vanish for large x_1 simply because the edge profile interpolates between two facets at $x_1=\pm\infty$ (recall that the facet surface current is zero). Thus, $J_1=0$, and, with Eq. (B10),

$$0=-\frac{\partial U(M_1,\alpha)}{\partial M_1}+\kappa\frac{d^2M_1}{dx_1^2}. \tag{B13}$$

Equation (B13) is analogous to the equation of motion of a particle with position $M_1(x_1)$ in a one-dimensional potential $-U(M_1,\alpha)$; x_1 here is the ''time'' in this analogy. Using Eq. (B13), one has the ''conservation of energy'' equation

$$0=\frac{d}{dx_1}\left[\frac{\kappa}{2}\left(\frac{dM_1}{dx_1}\right)^2-U(M_1(x_1),\alpha)\right]. \tag{B14}$$

By integrating Eq. (B14),

$$\frac{\kappa}{2}\left(\frac{dM_1}{dx_1}\right)^2-U(M_1(x_1),\alpha)=-U_{\min}. \tag{B15}$$

Here, $U_{\min}$ signifies the absolute minimum of $U(M_1,M_2)$. This choice of integration constant is appropriate here because, for large $|x_1|$, the slope approaches a facet slope [recall that facet slopes minimize the local potential $U(M_1,M_2)$]. Equation (B15) will give us an edge profile in the coordinate system in which the x_1 axis is perpendicular to the edge and the x_2 axis is along the edge, as already described in Sec. IX. As in Sec. IX, let 2ϕ be the angle between the facet n and n' that intersect at the edge. $|\mathbf{M}_n|=|\mathbf{M}_{n'}|=M_0$, whereas $\mathbf{M}_n=[-M_0\sin(\phi),+M_0\cos(\phi)]$ and $\mathbf{M}_{n'}=[+M_0\sin(\phi),+M_0\cos(\phi)]$.

The edge slope vector in Eq. (B9) asymptotically approaches those of the facets, i.e., for $x_1\to-\infty$, $\mathbf{M}=[M_1(x_1),\alpha]\to\mathbf{M}_n=[-M_0\sin(\phi),M_0\cos(\phi)]$, whereas, for $x_1\to+\infty$, $\mathbf{M}=[M_1(x_1),\alpha]\to\mathbf{M}_{n'}=[M_0\sin(\phi),M_0\cos(\phi)]$. In both of these limits, $U(\mathbf{M})\to U(\mathbf{M}_n)=U(\mathbf{M}_{n'})=U_{\min}$. At the very edge, $M_1=0$, and $\mathbf{M}=[0,\alpha]=[0,M_0\cos(\phi)]$. Thus, $\alpha=M_0\cos(\phi)$ is the interface slope at surface points on the edge. The overall edge profile can be obtained by integrating Eq. (B15), i.e.,

$$\sqrt{\frac{\kappa}{2}}\,\frac{dM_1}{dx_1}=\sqrt{U(M_1(x_1),\alpha)-U_{\min}}, \tag{B16}$$

by writing

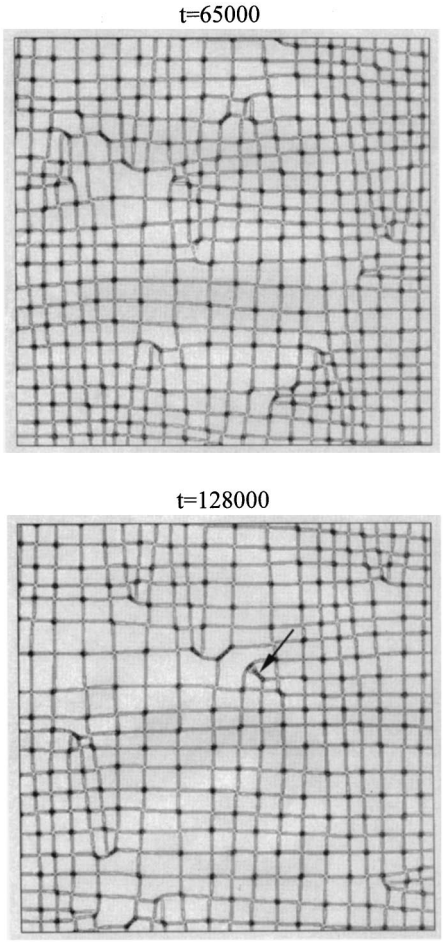

FIG. 19. The same as in Fig. 15, here at times $t=65\,000$ and $t=128\,000$. The arrow points to an unstable bound state between two dislocations moving in different directions, one vertically, the other one horizontally.

$$dx_1 = \sqrt{\frac{\kappa}{2}}\,\frac{dM_1}{\sqrt{U(M_1,\alpha)-U_{\min}}}, \tag{B17}$$

and integrating both sides of this equation. Equation (B17) with $\alpha = M_0\cos(\phi)$, was used to obtain the edge profiles quoted in Sec. IX.

The edge effective free energy [in reference to the infinite facet ground state] is, by Eq. (B2),

$$\begin{aligned} F_{\text{edge}} &= \int\int dx_1 dx_2 \left[U(M_1,M_2)-U_{\min} + \frac{\kappa}{2}\left(\frac{\partial M_1}{\partial x_1}+\frac{\partial M_2}{\partial x_2}\right)^2\right] \\ &= \int\int dx_1 dx_2 \left[U(M_1(x_1),\alpha) - U_{\min} + \frac{\kappa}{2}\left(\frac{dM_1(x_1)}{dx_1}\right)^2\right] \\ &= l_{\text{edge}}\cdot\sigma, \end{aligned} \tag{B18}$$

where l_{edge} is the edge length (along the x_2 direction), and σ is the edge line tension,

$$\sigma = \int_{-\infty}^{+\infty} dx_1 \left[U(M_1(x_1),\alpha)-U_{\min} + \frac{\kappa}{2}\left(\frac{dM_1(x_1)}{dx_1}\right)^2\right]. \tag{B19}$$

Using Eq. (B15), we see that the edge line tension σ in Eq. (B19) can be written also as

$$\sigma = 2\int_{-\infty}^{+\infty} dx_1 [U(M_1(x_1),\alpha)-U_{\min}], \tag{B20}$$

or, as

$$\sigma = \kappa\int_{-\infty}^{+\infty} dx_1 \left(\frac{dM_1}{dx_1}\right)^2. \tag{B21}$$

By using Eq. (B17) one can turn the integration over x_1 in Eq. (B20) into an integration over M_1. This yields

$$\sigma = 2\int \sqrt{\frac{\kappa}{2}}\,\frac{dM_1}{\sqrt{U(M_1,\alpha)-U_{\min}}}\cdot[U(M_1,\alpha)-U_{\min}]. \tag{B22}$$

Here, as noted before, $\alpha = M_0\cos(\phi)$, whereas M_1 changes between $-M_0\sin(\phi)$ (for $x_1\to-\infty$) and $+M_0\sin(\phi)$ (for $x_1\to+\infty$). Thus,

$$\sigma = \sqrt{2\kappa}\int_{-M_0\sin(\phi)}^{+M_0\sin(\phi)} dM_1 \times\sqrt{U(M_1,M_2=M_0\cos(\phi))-U_{\min}}. \tag{B23}$$

Equation (B23) has been used to calculate the results for edge tensions quoted in Sec. IX.

By Eq. (B11), we see that the edge carries a nonzero surface current which flows along the edge,

$$J_2(x_1) = J_2^{\text{NE}}(M_1(x_1),M_2=M_0\cos(\phi)). \tag{B24}$$

This current vanishes for large x_1 where the edge slope approaches a facet slope. Edges thus act as thin wires transporting the surface current. The net current flux transported by the edge is

$$I_{\text{edge}} = \int_{-\infty}^{+\infty} dx_1 J_2^{\text{NE}}(M_1(x_1),M_2=M_0\cos(\phi)). \tag{B25}$$

Again, with Eq. (B17) one can turn the integration over x_1 in Eq. (B25) into integration over M_1. Thus,

$$I_{\text{edge}} = \sqrt{\frac{\kappa}{2}}\int_{-M_0\sin(\phi)}^{+M_0\sin(\phi)} \times\frac{dM_1}{\sqrt{U(M_1,M_2=M_0\cos(\phi))-U_{\min}}} \times J_2^{\text{NE}}(M_1,M_2=M_0\cos(\phi)),$$

or, as $J_2 = -\partial U(M_1,M_2)/\partial M_2$,

$$I_{\rm edge} = -\sqrt{\frac{\kappa}{2}} \int_{-M_0 \sin(\phi)}^{+M_0 \sin(\phi)} \left[\frac{dM_1}{\sqrt{U(M_1,M_2)-U_{\rm min}}} \times \frac{\partial}{\partial M_2} U(M_1,M_2) \right]_{M_2 = M_0 \cos(\phi)} .$$

This expression is identical to

$$I_{\rm edge} = -\sqrt{2\kappa} \int_{-M_0 \sin(\phi)}^{+M_0 \sin(\phi)} dM_1 \times \left(\frac{\partial}{\partial M_2} \sqrt{U(M_1,M_2)-U_{\rm min}} \right)_{M_2 = M_0 \cos(\phi)} . \quad \text{(B26)}$$

Equation (B26) has been used to calculate the results for the edge surface currents quoted in Sec. IX.

APPENDIX C

Here, in Figs. 15–19, we give a time sequence (10 frames) of the evolution of the network of edges for the square symmetry (001) surfaces (on a 300×300 portion of the 1000×1000 system). The two types of edges described in Sec. VII, regular edges [oriented parallel to the x and y axis] and rooftop edges [oriented parallel to $y=\pm x$ axis] are clearly visible here. Also, it is obvious that the edges form nearly regular lattices [edge crystals] occasionally disordered by dislocation defects. Note that each dislocation incorporates a rooftop edge at its core. In fact, most of the rooftop ridges are incorporated into dislocation cores.

The sequence in Figs. 15–19 gives insight into the mechanism and the dynamics of the coarsening process on the square symmetry (001) surfaces. The processes of dislocation motion and dislocation annihilations that we invoked in Sec. VIII, where we proposed the kinetic scaling theory of the MBE growth, are documented in these ten snapshots. Figures 15–19 show, in a quick look, that indeed there is a coarsening going on. The sequence is a good visualization tool to see how the coarsening proceeds. For example, by looking at the first time frame, at $t=16\,000$, and the last one, at $t=126\,000$, we notice that lattice constant of the nearly periodic network of edges has visibly increased, whereas the density of the dislocations has decreased substantially.

In some of these figures, we see also occasional formations of unstable bound states between two dislocations moving in different directions, one vertically, the other one horizontally. See, for example, Fig. 19, at $t=128\,000$.

[1] See, for example, J. Y. Tsao, *Materials Fundamentals of Molecular Beam Epitaxy* (World-Scientific, Singapore, 1993).
[2] G. Ehrlich and F. G. Hudda, J. Chem. Phys. **44**, 1039 (1966).
[3] R. L. Schwoebel and E. J. Shipsey, J. Appl. Phys. **37**, 3982 (1966); R. L. Schwoebel, *ibid.* **40**, 614 (1969).
[4] J. Villain, J. Phys. I **1**, 19 (1991).
[5] H.-J. Ernst, F. Fabre, R. Folkerts, and J. Lapujoulade, Phys. Rev. Lett. **72**, 112 (1994).
[6] M. D. Johnson, C. Orme, A. W. Hunt, D. Graff, J. Sudijono, L. M. Sander, and B. G. Orr, Phys. Rev. Lett. **72**, 116 (1994).
[7] J. W. Evans, D. E. Sanders, P. A. Thiel, and A. E. DePristo, Phys. Rev. B **41**, 5410 (1990); J. W. Evans, *ibid.* **43**, 3897 (1993).
[8] D. D. Vvedensky, A. Zangwill, C. N. Luse, and M. R. Wilby, Phys. Rev. E **48**, 852 (1993).
[9] M. Siegert, in *Scale Invariance, Interfaces, and Non-Equilibrium Dynamics*, edited by A. J. McKane, M. Droz, J. Vannimenus, and D. Wolf, NATO ASI Series B Vol. 344 (Plenum, New York, 1995), pp. 165–202.
[10] M. C. Bartelt and J. W. Evans, Phys. Rev. Lett. **75**, 4250 (1995).
[11] G. W. Smith, A. J. Pidduck, C. R. Whitehouse, J. L. Glasper, and J. Spowart, J. Cryst. Growth **127**, 996 (1993); C. Orme, M. D. Johnson, K.-T. Leung, B. G. Orr, P. Smilauer, and D. Vvedensky, *ibid.* **150**, 128 (1995).
[12] J. E. Van Nostrand, S. J. Chey, M.-A. Hasan, D. G. Cahill, and J. E. Greene, Phys. Rev. Lett. **74**, 1127 (1995).
[13] K. Thurmer, R. Koch, M. Weber, and K. H. Rieder, Phys. Rev. Lett. **75**, 1767 (1995).
[14] J. A. Stroscio, D. T. Pierce, M. Stiles, A. Zangwill, and L. M. Sander, Phys. Rev. Lett. **75**, 4246 (1995).
[15] F. Tsui, J. Wellman, C. Uher, and R. Clarke, Phys. Rev. Lett. **76**, 3164 (1996).
[16] M. Siegert and M. Plischke, Phys. Rev. Lett. **73**, 1517 (1994).
[17] J. Amar and F. Family, Phys. Rev. B **54**, 14 742 (1996).
[18] A. J. Bray, Adv. Phys. **34**, 357 (1994).
[19] W. W. Mullins, J. Appl. Phys. **28**, 333 (1957), in *Metal Surfaces: Structure, Energetics and Kinetics* (American Society for Metals, Metals Park, OH, 1963), p. 17.
[20] L. Golubovic and R. P. U. Karunasiri, Phys. Rev. Lett. **66**, 3156 (1991).
[21] L. Golubovic, Phys. Rev. Lett. **78**, 90 (1997); The effective free energy discussed here does not include ''vertical asymmetry'' between mound tops and valleys that can be modeled by including Villain–Das Sarma and like terms in the equation of motion [see, e.g., Z. W. Lai and S. Das Sarma, Phys. Rev. Lett. **66**, 2348 (1991)]. Here we adopt the attitude of considering these symmetry-breaking terms to be irrelevant for the late time coarsening behavior (as, e.g., in Refs. [16] and [22]). Nonetheless, more detailed investigations are needed to verify the nature and generality of this irrelevance of the symmetry-breaking terms. At this place, we remark that vertical asymmetry can be incorporated by adding suitably defined terms into the effective free energy.
[22] M. Siegert, Physica A **239**, 420 (1997); M. Siegert, Phys. Rev. Lett. **81**, 5481 (1998).
[23] J. Amar, Phys. Rev. B **60**, R11 317 (1999).
[24] L. Golubovic, D. Moldovan, and A. Peredera, Phys. Rev. Lett. **81**, 3387 (1998); L. Golubovic, D. Moldovan, and A. Peredera, Phys. Rev. E **61**, 1703 (2000).
[25] D. Moldovan and L. Golubovic, Phys. Rev. Lett. **82**, 2884 (1999); D. Moldovan and L. Golubovic, Phys. Rev. E **60**, 4377 (1999).